

Modal Acoustic Velocimetry in libration-driven flows

Henri-Claude Nataf^{1*}, Sylvie Su², Philippe Roux¹,
Philippe Cardin¹, David Cébron¹, Yann Do¹

^{2*}Univ. Grenoble Alpes, CNRS, IRD, Univ. Gustave Eiffel, ISTERre,
38000, Grenoble, France.

²Normandie Univ, UNIROUEN, INSA Rouen, CNRS, CORIA, 76000,
Rouen, France.

*Corresponding author(s). E-mail(s):

Henri-Claude.Nataf@univ-grenoble-alpes.fr;

Contributing authors: sylvie.su@univ-rouen.fr; Philippe.Roux@univ-grenoble-alpes.fr;
Philippe.Cardin@univ-grenoble-alpes.fr;
David.Cebbron@univ-grenoble-alpes.fr; Yann.Do@univ-grenoble-alpes.fr;

Abstract

Flows in rapidly spinning bodies, such as the iconic libration-induced flow, are key ingredients of the dynamics of stars and planetary interiors. Laboratory experiments of such flows experience a strong centrifugal acceleration, which forbids the use of classical velocimetry methods relying on particle tracking. Modal Acoustic Velocimetry was introduced by [Triana et al. \(2014\)](#) as a new particle-free method, inspired from helioseismology, to alleviate this problem. In this method, acoustic modes are excited in the fluid and recorded in the spinning container. Rotation and fluid flow modify the characteristics of these modes, lifting the degeneracy of non-axisymmetric modes. To date, this method has only been applied to stationary or statistically stationary flows, by measuring frequency splittings in the spectral domain. Here, we analyze time-varying libration-induced flows. We propose and test two data acquisition strategies. The first strategy operates in the frequency domain and relies on the periodicity of the flow, while the second strategy involves a high-resolution algorithm applied in the time domain. The retrieved mode frequency splittings are compared to those computed for a classical linear libration-induced flow model ([Greenspan 1968](#)). A very good agreement is obtained, but we observe an unexpected time delay, which we attribute to the buildup time of acoustic modes. We retrieve more than 50 splitting measurements at 10 successive libration phases. Inverting these data with the SOLA method,

often used in helioseismology, we derive profiles (1D-inversion) and maps (2D-inversion) of the azimuthally-averaged fluid rotation rate. The inversions recover the main characteristics of this time-dependent flow. The 2D-inversion confirms the invariance of the flow along the rotation axis. Resolution kernels show that flow can be mapped on patches that spread over approximately 5% of a meridian quarter-plane. Our study paves the way to the investigation of more exotic regimes of precession- or libration-induced flows.

Keywords: Modal Acoustic Velocimetry, libration, spheroid, acoustics, SOLA, inversion

1 Introduction

Over time, Particle Image Velocimetry (PIV) has emerged as the predominant method for examining velocity fields in fluids (e.g., [Adrian and Westerweel 2011](#); [Raffel et al. 2018](#)). However, PIV relies on the presence of light and particles. In situations where light cannot penetrate the fluid, such as in liquid metals, Ultrasonic Doppler Velocimetry (UDV) serves as an effective alternative ([Brito et al. 2001](#); [Eckert and Gerbeth 2002](#); [Brito et al. 2011](#)), though it still requires particles to backscatter ultrasounds. This is a problem in rapidly spinning experiments, in which it is almost impossible to prevent particles to settle under the centrifugal acceleration. Such experiments are central in the exploration of the dynamics of planetary interiors (see [Pothérat and Horn \(2024\)](#) for a recent review), hence the need for non-intrusive particle-free methods. Good results have been obtained from ultrasonic time-of-flight in liquid metal ([Burmahn et al. 2022](#)), but the integrated data it provides limits its application.

In the mean time and for quite a while, astrophysicists have been inferring flows in the Sun and other stars from their acoustic signature, developing the new disciplines of helioseismology ([Gough and Toomre 1991](#); [Thompson et al. 2018](#)) and asteroseismology ([Aerts et al. 2010](#)), building upon the fundamentals of seismology. The idea of applying these approaches to experiments in fluids was pioneered by [Triana et al. \(2014\)](#) who set the basics of Modal Acoustic Velocimetry (MAV) and provided a proof-of-concept with data obtained in a spherical Couette flow. MAV was further extended by [Su et al. \(2020\)](#) who provided the first measurements of the Ledoux coefficients in a rapidly spinning spheroid. The Ledoux coefficients ([Ledoux 1951](#)) quantify the splitting of acoustic normal modes produced by the Coriolis acceleration in a bounded fluid, such as a star.

Our study pursues the development of MAV by investigating an iconic time-varying flow: the flow induced by longitudinal libration. We adapted the ZoRo experiment ([Su et al. 2020](#)) to produce and characterize libration-induced flows. We designed and tested two different acquisition strategies to apply Modal Acoustic Velocimetry for flows produced by longitudinal libration in a rapidly spinning gas-filled spheroid. A brief description of libration-induced flows is given in this introduction, which also recalls the basics of Modal Acoustic Velocimetry, and presents the ZoRo setup.

1.1 Libration basics

Libration-induced flows in rapidly spinning spheres and spheroids have received a lot of attention because of their geophysical and planetary relevance (Aldridge 1967; Tilgner 1999; Comstock and Bills 2003; Noir et al. 2009; Busse 2010; Le Bars et al. 2015; Cébron et al. 2021). For longitudinal libration, the instantaneous rotation frequency $f_{shell}(t)$ of a gas-filled shell can be written as:

$$f_{shell}(t) = f_o + \Delta f \sin(2\pi f_{lib} t), \quad (1)$$

where f_o , Δf , and f_{lib} denote the average shell rotation rate, libration amplitude, and libration frequency, respectively. We will only consider cases with $\Delta f \ll f_o$ and $f_{lib} \ll f_o$, allowing to neglect non-linear effects and the harmonic modulation of the boundary-layer flow, respectively.

This shell motion can be regarded as a continuous succession of infinitesimal spin-up and spin-down forcings, which have been studied in detail by Greenspan and co-workers (Greenspan and Howard 1963; Greenspan 1968).

In the asymptotic regime corresponding to rapid rotation and small libration amplitude, the induced flow obeys Proudman-Taylor constraint, and is thus z -independent (where z marks the coordinate along the rotation axis) except in a thin viscous boundary layer beneath the shell, the Ekman layer.

In an axisymmetric shell spinning around its symmetry axis, fluid flow is then a function of cylindrical radius and time only. Following Deleplace (2005, p.42-46), the fluid rotation rate $f_{fluid}(s, t)$ in the spinning frame is then obtained as

$$\frac{f_{fluid}(s, t)}{\Delta f} = \frac{\xi}{\sqrt{1 + \xi^2}} \sin \left(2\pi f_{lib} t + \pi + \arctan \frac{1}{\xi} \right), \quad (2)$$

where the expression of ξ depends on the geometry of the shell. For a sphere of radius r_o , it is given by

$$\xi = \frac{f_{lib}}{f_{Ekman}} (1 - s^2)^{3/4}, \quad (3)$$

where s is the cylindrical radius, normalized by r_o and

$$\frac{f_{Ekman}}{f_o} = \sqrt{\frac{2\pi\nu}{f_o r_o^2}} = 2\pi \text{Ek}^{1/2},$$

where ν is the kinematic viscosity of the fluid, and $\text{Ek} = \nu/(2\pi f_o r_o^2)$ is the Ekman number. The expression of ξ for an axisymmetric spheroid is derived in Appendix A.

Figure 1 shows the fluid rotation rate f_{fluid} predicted by Eq. 2 with $f_{lib}/f_{Ekman} = 0.266$, which corresponds to $f_{lib} = 0.05$ Hz for the ZoRo experiment filled with air at normal conditions ($\nu = 1.5 \times 10^{-5} \text{ m}^2 \text{ s}^{-1}$), spinning at $f_o = 15$ Hz. Dimensionless fluid flow rotation rate $f_{fluid}(s, t)/\Delta f$ is contoured in an s - t map, with time t normalized by $T_{lib} = 1/f_{lib}$.

As the shell accelerates from $f_{shell} = f_o$ at $t = 0$, the fluid spin rate in the shell reference frame is small near the equator ($s/r_o = 1$) but reaches a minimum closer to

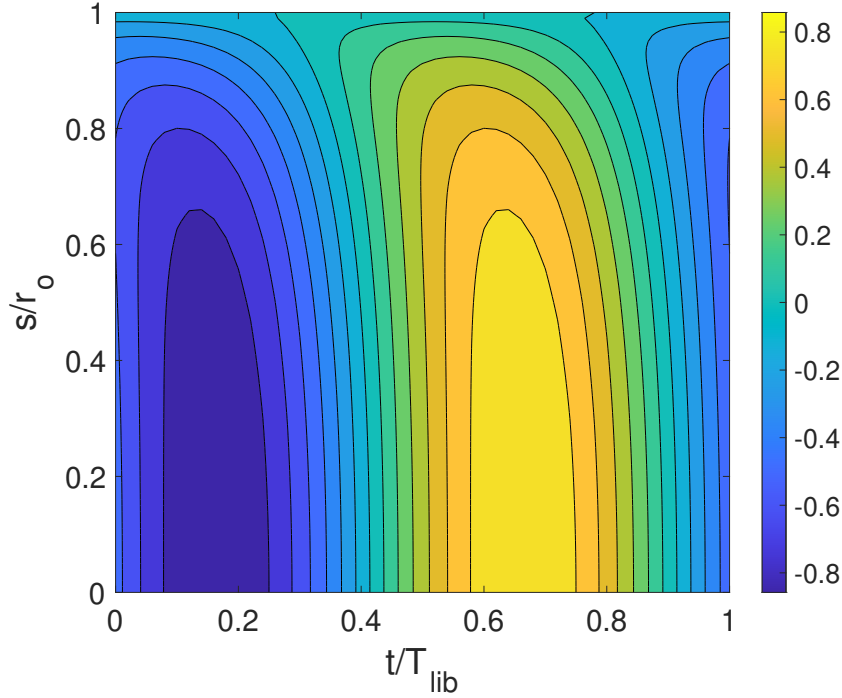


Fig. 1 Isocontours of normalized fluid rotation rate $f_{fluid}/\Delta f$ as a function of time and cylindrical radius, as predicted by Greenspan's theory for libration in a rapidly spinning sphere, with $f_{lib}/f_{Ekman} = 0.266$. Fluid rotation rate is expressed in the spinning shell reference frame. Cylindrical radius and time are normalized by r_o and T_{lib} , respectively.

the spin axis, where the fluid has not felt yet the shell acceleration. This minimum is reached before f_{shell} reaches its maximum (at $t/T_{lib} = 1/4$) and its amplitude is smaller than Δf because libration is slow enough to be transmitted all the way to the core of the fluid.

Another representation is proposed in Fig. 2, where s -profiles of the fluid rotation rate (in the librating shell frame) are shown at different libration phases every 36° from 0° to 324° . Crosses give the same quantities as measured in the equatorial plane of an axisymmetric numerical simulation performed in the spherical geometry, using the XSHELLS package (Schaeffer 2013; Kaplan et al. 2017), with $\Delta f = 1.5$ Hz and $Ek = 4 \times 10^{-6}$. The differences between the finite amplitude numerical simulation and the analytical asymptotic expression are very small in this parameter range. For large libration amplitudes Δf , longitudinal rolls develop in the Ekman boundary layer during the spin-down phase of the libration cycle (Noir et al. 2009). These rolls are clearly observed in axisymmetric numerical simulations when increasing Δf to 3.6 Hz.

In this article, we restrict our attention to the stable regime for which Greenspan's asymptotic theory should provide an excellent flow prediction.

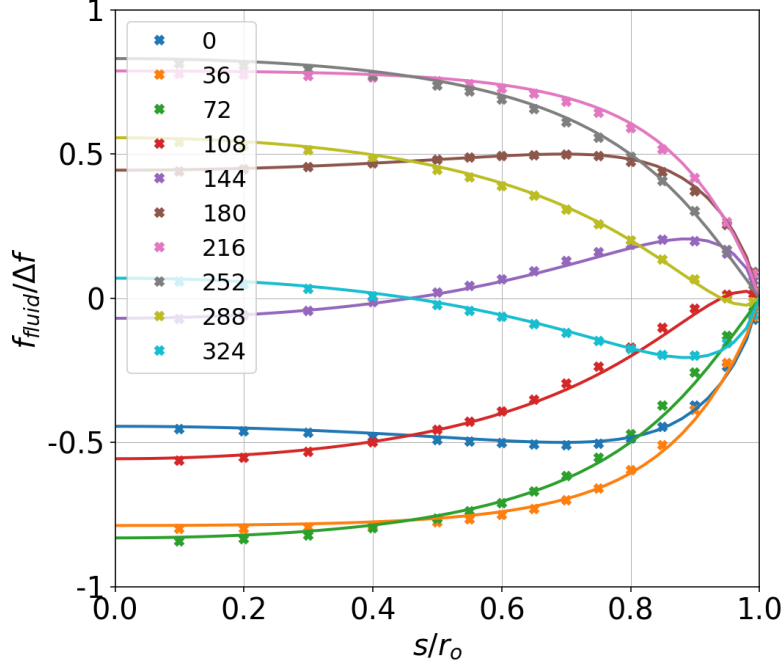


Fig. 2 Same libration flow as in Figure 1, corresponding to $f_o = 15$ Hz, $f_{lib} = 0.05$ Hz and $\Delta f = 1.5$ Hz in the ZoRo experiment. Solid lines show fluid rotation rate as a function of cylindrical radius from Greenspan's theory, for selected libration phases from 0° to 324° in 36° -steps. Crosses are the corresponding fluid rotation rates measured in the equatorial plane of an axisymmetric numerical simulation ($Ek = 4 \times 10^{-6}$).

1.2 Basics of Modal Acoustic Velocimetry

As we mentioned, Modal Acoustic Velocimetry was introduced by [Triana et al. \(2014\)](#) as a new method to measure flow velocity in fluid-filled cavities. MAV is inspired by helioseismology and proves useful in experiments where particles cannot be employed, such as in rapidly spinning spheres or spheroids ([Triana et al. 2014](#); [Mautino 2016](#); [Su et al. 2020](#); [Su 2020](#); [Vidal et al. 2020](#)). The method consists in exciting the acoustic normal modes of the fluid in the cavity, and measuring for each mode the frequency shift induced by solid body rotation and fluid flow. Previous works ([Triana et al. 2014](#); [Mautino 2016](#); [Su et al. 2020](#); [Su 2020](#)) focused on stationary or statistically stationary flows. Acoustic modes can then be excited by long-lasting chirps, covering a wide frequency range and providing a fine frequency resolution. It is important to extend MAV to time-dependent flows, which requires devising alternative appropriate strategies.

1.2.1 Acoustic modes

We briefly recall here a few basic properties of acoustic modes in a gas-filled spheroid. More details can be found in [Ledoux \(1951\)](#); [Moldover et al. \(1986\)](#); [Mehl \(2007\)](#); [Aerts et al. \(2010\)](#); [Triana et al. \(2014\)](#); [Su et al. \(2020\)](#); [Vidal et al. \(2020\)](#). Starting from

a gas contained in a rigid spherical shell, we recall that acoustic modes are quantized. The pressure field of a resonant acoustic mode can be written as:

$$p(r, \theta, \phi) = {}_nR_l(r) Y_l^m(\theta, \phi), \quad (4)$$

where $Y_l^m(\theta, \phi)$ is the spherical harmonic of degree l and order m , which describes the surface variation of the mode's pressure field. Spherical coordinates θ and ϕ are the usual colatitude and longitude, respectively. Radius r is normalized by the shell inner radius r_o . Index n gives the number of zeroes of function ${}_nR_l(r)$, which provides the radial variation of the mode's pressure field, and is given by ${}_nR_l(r) = j_l({}_nk_l r)$, where j_l is the spherical Bessel function of the first kind, of degree l . The radial wave number ${}_nk_l$ is such that, for a rigid shell, ${}_nR_l'|_{r=1} = 0$ (no radial wave displacement at the solid shell boundary), where the prime represents the r -derivative. Every triplet of integers (n, l, m) defines an acoustic mode, or *singlet*, which we denote ${}_nS_l^m$. Each mode resonates at a specific frequency ${}_nf_l^m$. In a sphere of radius r_o , frequencies are m -degenerate: ${}_nf_l^m = {}_nf_l = {}_nk_l c / (2\pi r_o)$ for all m , with c the sound velocity of the gas.

In a spheroid, this m -degeneracy is partly lifted, but *doublets* ${}_nS_l^{\pm m}$ still have the same frequency. Global rotation and/or azimuthal flows lift this remaining degeneracy. MAV thus measures the frequency difference between singlets ${}_nS_l^{-m}$ and ${}_nS_l^m$ to retrieve global axisymmetric maps of azimuthal flow velocity.

Following Su et al. (2020), we compute predicted mode frequencies ${}_nf_l^m$ by perturbation theory to the second order in ellipticity, in order to obtain the right ordering of the doublets. Note that the projection on spherical harmonics is an approximation in the spheroidal case, and only applies for moderate flattening. See Su et al. (2020) for details, and Vidal et al. (2020) for a more complete and rigorous presentation. One limitation of the shape perturbation theory we use (Mehl 2007) is that it does not provide the eigen function perturbation. However, the flattening of ZoRo is small enough that using the spherical eigen modes is appropriate. A method for computing pressure fields at higher-order in ellipticity is presented in Albo et al. (2010). We now turn to the computation of mode splitting produced by an axisymmetric azimuthal flow or fluid rotation rate $f_{fluid}(r, \theta)$.

1.2.2 2D flow velocity kernels

Following Triana et al. (2014), we express the difference $\delta f_{{}_nS_l^{\pm m}}$ between the frequencies of singlets ${}_nS_l^{-m}$ and ${}_nS_l^m$ as a function of the rotation rate $f_{fluid}(r, \theta)$ of the axisymmetric flow by:

$$\delta f_{{}_nS_l^{\pm m}} = 2m \int_0^1 \int_0^\pi {}_nK_l^m(r, \theta) f_{fluid}(r, \theta) r dr d\theta, \quad (5)$$

where sensitivity kernel ${}_nK_l^m(r, \theta)$ is given by:

$${}_nK_l^m(r, \theta) = \frac{r \sin \theta}{{}_nI_l} \left\{ \xi_r^2 p^2 + \xi_h^2 \left[q^2 + \frac{m^2}{\sin^2 \theta} p^2 - 2 \frac{pq}{\tan \theta} \right] - 2 \xi_h \xi_r p^2 \right\}, \quad (6)$$

with:

$$p = P_l^m(\cos \theta), \quad q = \frac{dP_l^m(\cos \theta)}{d\theta}, \quad \xi_r = \frac{d[nR_l(r)]}{dr} \quad \text{and} \quad \xi_h = \frac{nR_l(r)}{r}, \quad (7)$$

where $P_l^m(\cos \theta)$ is the associated Legendre polynomial and ${}_nI_l$ a normalization integral:

$${}_nI_l = \int_0^1 [|\xi_r(r)|^2 + l(l+1)|\xi_h(r)|^2] r^2 dr. \quad (8)$$

The 2D sensitivity kernels ${}_nK_l^m(r, \theta)$ of the collection of 53 modes discussed in this article are displayed in Appendix B. Note that all kernels are positive and symmetrical with respect to the equator of the reference frame. Although we compute mode frequencies to the second order in ellipticity, we stick to kernels of the sphere in our inversions.

1.2.3 1D flow velocity kernels

Since Greenspan's flow is z -invariant, we integrate (r, θ) mode splitting kernels over z to get ${}_n\mathbb{K}_l^m(s)$ sensitivity kernels, in order to recover $f_{fluid}(s)$. We first express the 2D (r, θ) kernels in the (s, z) reference frame:

$${}_n\mathcal{K}_l^m(s, z) = {}_nK_l^m(r = \sqrt{s^2 + z^2}, \theta = \arctan(z/s)). \quad (9)$$

We then integrate over z to obtain the 1D ${}_n\mathbb{K}_l^m(s)$ sensitivity kernels:

$${}_n\mathbb{K}_l^m(s) = \int_{-h(s)}^{h(s)} {}_n\mathcal{K}_l^m(s, z) dz \quad \text{with} \quad h(s) = \sqrt{1 - s^2}, \quad (10)$$

which provides the frequency splitting $\delta f_{{}_nS_l^{\pm m}}$ of acoustic doublet ${}_nS_l^{\pm m}$ through:

$$\delta f_{{}_nS_l^{\pm m}} = 2m \int_0^1 {}_n\mathbb{K}_l^m(s) f_{fluid}(s) ds. \quad (11)$$

Figure 3 displays the 1D sensitivity kernels ${}_n\mathbb{K}_l^m(s)$ as a function of dimensionless cylindrical radius s for the collection of modes analyzed in this article. Note that kernels are not sharply localized and that sensitivity to fluid flow is obtained for $0.2 \lesssim s/r_o \lesssim 0.9$, all kernels dropping to 0 at $s/r_o = 0$ and $s/r_o = 1$.

1.3 The ZoRo experiment

The ZoRo experiment was set-up to investigate convective and mechanically induced flows in a rapidly spinning gas-filled spheroid. Such flows are observed or expected in the fluid envelopes of planets. The experiment consists in an aluminum shell that can spin around a vertical axis at rates up to 50 rotations per second. The shell can be filled with different gases (air, nitrogen, argon) kept at pressures between 0.3×10^5 and 4×10^5 Pa. The axisymmetric cavity has an equatorial radius $r_{eq} = 0.2$ m and polar

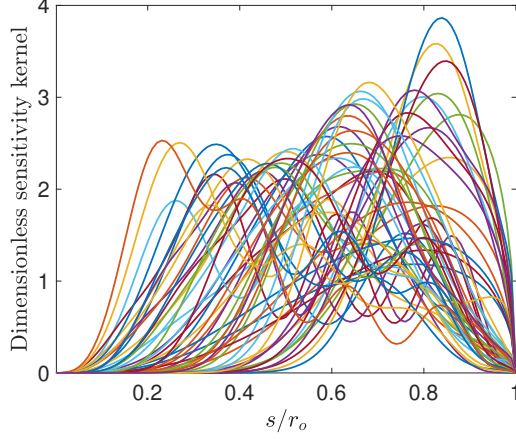


Fig. 3 Plot of 1D sensitivity kernels ${}_n\mathbb{K}_l^m(s)$ as a function of dimensionless cylindrical radius s for the collection of 53 acoustic doublets ${}_nS_l^{\pm m}$ analyzed in this article.

radius $r_{pol} = 0.19$ m. A sphere of the same volume has radius $r_o = \sqrt[3]{r_{eq}^2 r_{pol}} = 0.1966$ m.

The MAV technique was implemented in ZoRo since strong centrifugal effects disqualify particle-based techniques. The spinning shell is thus equipped with four loudspeakers and fourteen microphones. [Su et al. \(2020\)](#) describe the methodology developed to excite, measure, model, and process the acoustic modes of ZoRo. They also show measurements of acoustic mode splitting caused by the Coriolis force in solid body rotation, confirming the theory of [Ledoux \(1951\)](#). More details can be found in [Su et al. \(2020\)](#) and [Su \(2020\)](#).

Libration is produced by varying the instantaneous spin rate of the shell with time in a sinusoidal fashion. Particular care is given to the synchronization of the various measurements (see Appendix C for details). In ZoRo, the libration flow shown in Fig. 1 is obtained with $f_o = 15$ Hz and $f_{lib} = 0.05$ Hz, when it is filled with air at ambient pressure and temperature ($\nu = 1.5 \times 10^{-5} \text{ m}^2 \text{ s}^{-1}$). The Ekman number is then $\text{Ek} = 4 \times 10^{-6}$, yielding $f_{Ekman} = 0.188$ Hz, and the exponential thickness of the viscous layer beneath the shell, called the Ekman layer, is $\delta_{Ekman} = \sqrt{\nu/(2\pi f_o)} = 0.4$ mm.

Two MAV acquisition strategies are presented in section 2. Resulting experimental results are compared with theoretical predictions in section 3. The next sections present the inversion of the data to retrieve the fluid spin rate: section 4.2 presents the results of 1D SOLA inversion, while the ingredients and results of 2D SOLA inversion are given in section 4.3. Section 5 discusses the limitations and perspectives of our study, and we conclude in Section 6.

2 MAV strategies for time-periodic flows

Previous MAV exercises (Triana et al. 2014; Mautino 2016; Su et al. 2020) excited acoustic modes by playing long chirps covering a large frequency range, and retrieved mode frequencies from the Fourier transform of the recorded signals. This strategy is well fit for stationary flows or for retrieving the mean of a moderately fluctuating flow. For time-varying flows such as those generated by libration, one would like to capture acoustic signatures in a short time lapse, of the order of a second for the case shown in Fig. 1. From Nyquist’s theorem, frequency resolution would then be of the order of one Hertz.

However, we will see that these flows produce mode splittings that typically range from 0.5 Hz to 15 Hz. This suggests that a frequency resolution of 1 Hz is not sufficient to properly constrain the flow. Faced to this problem, we developed and tested two strategies, which we now present.

2.1 Long chirps repeated with a libration phase offset

Our first strategy is to play and record long chirps (typically ~ 90 seconds) covering the full frequency range we can access (500 to 5 000 Hz). We thus obtain Fourier power spectra with a resolution of the order of 0.01 Hz. Of course, flow evolves while the chirp is played, but a given mode is only excited at a given time, or rather during a short time lapse (typically less than 0.2 to 1 second). Keeping track of the evolution of libration phase during the chirp, the measured splitting of a given mode can then be attributed to a known libration phase. By repeating the same chirp at different initial libration phase we scan the evolution of each mode splitting with libration phase.

An example is shown in Fig. 4. Libration parameters are $f_o = 15$ Hz, $f_{lib} = 0.05$ Hz and $\Delta f = 1.5$ Hz, and we play an 82s-long chirp spanning from 500 to 5 000 Hz. This chirp is repeated 10 times. During one chirp, the setup experiences 4.1 libration periods. Successive chirps thus sample the libration flow with a phase shift of 36° . We compute the power spectrum of the signals recorded for each of the ten 82s-long chirps.

Figure 4a displays a zoom of the ten spectra focused on acoustic doublet ${}_1S_3^{\pm 3}$. As in Su et al. (2020), each spectrum is obtained following these steps: (i) since this doublet is equatorially symmetric (because $l - m$ is even), we first sum the time-records of pairs of equatorially symmetric microphones; (ii) we compute the power spectrum of three such summed time-records; (iii) we take the mean of these three power spectra. The libration phase of each mean power spectrum, as listed in the legend, is deduced from the time $t - t_0$ at which the central frequency of the doublet is played in the chirp, t_0 corresponding to a nul libration phase.

Figure 4b shows synthetic power spectra computed for the same libration phases, augmented by a 10° delay (for reasons to be discussed later). Each spectrum is built following these steps: (i) the theoretical frequencies of the ${}_1S_3^3$ and ${}_1S_3^{-3}$ singlets are obtained by convolving the acoustic velocity kernel ${}_1\mathbb{K}_3^3(s)$ of Eq. 10 with the theoretical libration-flow model $f_{fluid}(s, t)$ of Eq. 2 for the considered libration phase

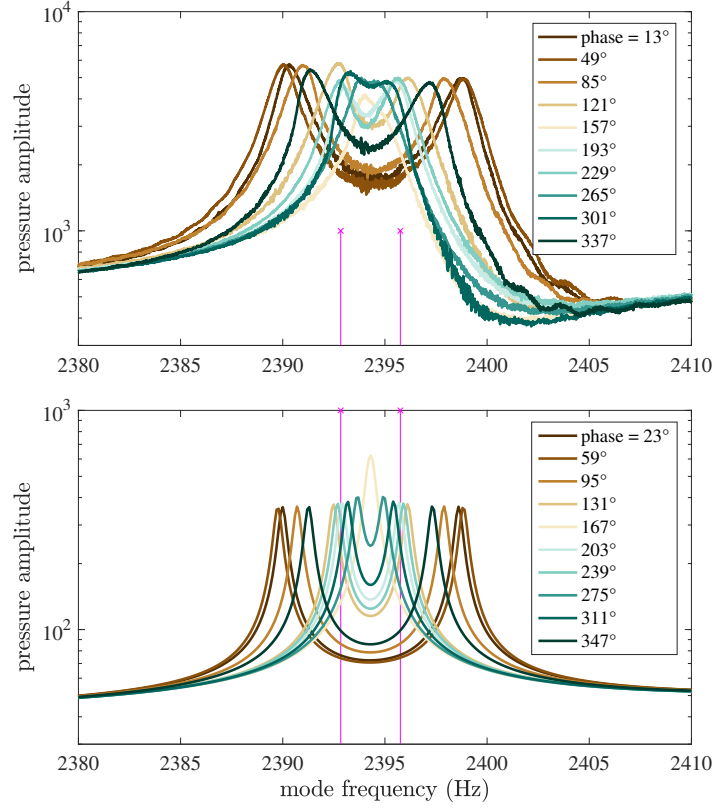


Fig. 4 Frequency spectra of split acoustic doublet ${}_1S_3^{\pm 3}$ for 10 successive libration phases, 36° apart. Libration parameters : $f_o = 15$ Hz, $f_{lib} = 0.05$ Hz and $\Delta f = 1.5$ Hz. (a) measured power spectra. The plot is a zoom centered at 2395 Hz of full spectra obtained by playing a 82s-long chirp spanning from 500 to 5 000 Hz. The legend indicates the libration phase achieved by the setup when the center frequency is played. (b) synthetic spectra computed from the splitting predicted by the convolution of the acoustic sensitivity kernel with Greenspan's libration flow model. Note that a phase delay of 10° has been added to the synthetics as compared to the measured data. The two magenta stems mark the frequencies of the ${}_1S_3^3$ and ${}_1S_3^{-3}$ singlets for solid body rotation of the fluid with the shell at spin rate f_o .

$2\pi f_{lib}(t-t_0)$; (ii) the acoustic power spectrum is computed by convolving each singlet's resonance lines with a Lorentzian (Su et al. 2020).

In this figure, the largest splitting is obtained for a libration phase of 59° . From Fig. 1 and 2, we see that the fluid rotation rate (in the spinning shell frame) is retrograde and near its minimum at that phase. The splitting decreases as the libration phase increases, until a phase of 167° when a single frequency peak is observed. This occurs

when the splitting due to the fluid flow exactly cancels the (opposite) splitting due to the shell spin, which is indicated by the two magenta stems for a $f_o = 15$ Hz spin rate. As the fluid flow becomes positive (prograde) the two singlets cross each other, yielding a splitting that increases again to a secondary maximum at a phase of 347° .

The exact same evolution is observed in Fig. 4a. The main difference is the width of the resonance peaks, which is larger than expected from theory, some widening being probably due to the evolution of the flow during the resonance buildup.

Our phase-offset long chirp strategy then consists in measuring the frequency splitting of as many doublets as possible for ten successive libration phases.

For each doublet, the splitting estimate and its error bar are obtained with the following steps (Su et al. 2020): (i) ‘plus’ and ‘minus’ time-records are obtained from the sum and difference of sound recorded by four pairs of equatorially-symmetric microphones (${}_nS_l^{\pm m}$ doublets with even $l - m$ show up in ‘plus’ records, while those with odd $l - m$ are seen in ‘minus’ records); (ii) ‘plus’ and ‘minus’ records are Fourier transformed; (iii) the resulting four ‘plus’ power spectra are averaged yielding ‘mean+’ power spectrum, and ‘mean-’ is obtained similarly; (iv) doublets ${}_nS_l^{\pm m}$ are identified in these spectra with the help of synthetic spectra, and a windowed spectrum is extracted together with a first estimate of mode splitting; (v) individual synthetic spectra are built varying four of their constitutive ingredients: doublet’s peak-to-peak splitting, doublet’s mean frequency, doublet’s amplitude, and singlets’ peak width; (vi) a grid search on these four elements provides the best splitting and its error bar.

This strategy only applies to time-periodic flows and requires that the played chirp largely dominates over other noise sources.

2.2 Short chirps and high-resolution frequency analysis

We developed a second strategy: play a short chirp centered on the frequency of a single acoustic doublet. Fluid rotation splits this doublet into two singlets with slightly different frequencies. The time-domain record of a given microphone thus consists in the superposition of two sine signals with slightly different periods. A one second-long record contains thousands of cycles, enough to detect and measure the two frequencies with a precision of 0.01 Hz. In other words, while obtaining the full frequency spectrum is limited by Nyquist theorem, this limit vanishes when the signal consists in the sum of a small number of sines that we wish to retrieve.

Processing follows a variant of the IRWIN method presented by Roux et al. (2004) and Philippe et al. (2008). The main ingredients of this method are recalled in Appendix E. For our application, the following steps are taken: (i) a short chirp (lasting typically less than 1 second) is repeatedly played on one or two loudspeakers, covering the resonance frequency range of a targeted doublet. (ii) we compute the auto-correlation of each record. (iii) we choose the number of monochromatic components to be searched for, and the frequency interval for the search. (iv) we launch an ensemble of inversions. (v) we gather the results in histograms that count the number of times each frequency has been recovered in the ensemble. One or two peaks normally stand up, yielding the singlets’ frequencies and their error bar. (vi) the procedure is

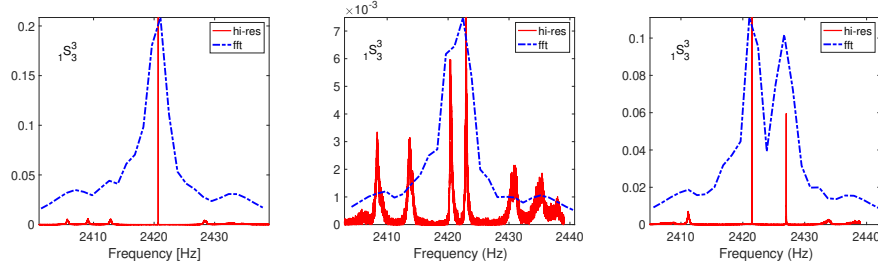


Fig. 5 Examples of the high-resolution analysis. Histograms (in red) of frequencies recovered by the iterative IRWIN algorithm for doublet ${}_1S_3^3$ at three different libration phases. The dot-dashed blue line gives the standard Fourier spectrum computed for each 0.82s-long time window.

repeated for the following chirps, probing successive phases of the libration-induced flow.

Figure 5 illustrates the performance of our high-resolution algorithm for three different libration phases for doublet ${}_1S_3^{\pm 3}$. While Nyquist theorem limits the frequency resolution of the standard power spectrum (dot-dash blue line) of our 0.82s-long time window, the high-resolution algorithm (red) isolates one or two frequencies very precisely in the time-domain signals. The middle panel shows a case when the algorithm only marginally recovers the frequencies.

The main limitation of this technique is that only a limited number of doublets can be targeted at the same time. We obtained good results with up to four simultaneous doublets, but the examples shown below target a single doublet. A great advantage of this method is that it can be used to probe non-periodic time-varying flows.

3 Comparing observations and synthetics

We give here examples of measurements obtained with both strategies. The data are compared with predictions computed by convolving the time-dependent fluid flow with the kernel of each acoustic mode. Fluid flow $f_{fluid}(s, t)$ is computed using the linear geostrophic theory of Greenspan and Howard (1963) adapted to libration in a spheroid, namely from Eq. 2 and A2. Note that we often replace time t by the libration phase $\phi(t) = 2\pi f_{lib} t \pmod{2\pi}$. The acoustic kernel ${}_n\mathbb{K}_l^m(s)$ provides the frequency splitting $\delta f_{{}_nS_l^{\pm m}}(t)$ of acoustic doublet ${}_nS_l^{\pm m}$ (see definition and expression in section 1.2.3). Note that although we compute mode frequencies by perturbation theory to second-order in ellipticity (Su et al. 2020), we use the acoustic kernels of a sphere.

3.1 Mode splitting collection from phase-offset chirps

We could measure the frequency splittings of some 53 doublets with the phase-offset long chirps strategy. Figure 6 compares results obtained for two chirp durations: 90 and 39 seconds. Libration parameters are: $f_o = 15$ Hz, $f_{lib} = 0.1$ Hz and $\Delta f = 1.5$ Hz. For each selected acoustic doublet ${}_nS_l^{\pm m}$, the measured splitting $\delta f_{{}_nS_l^{\pm m}}$ (frequency difference between spectral peaks of ${}_nS_l^{-m}$ and ${}_nS_l^{+m}$ singlets) is plotted as a function of libration phase. All splittings are first corrected for the effect of the Coriolis force

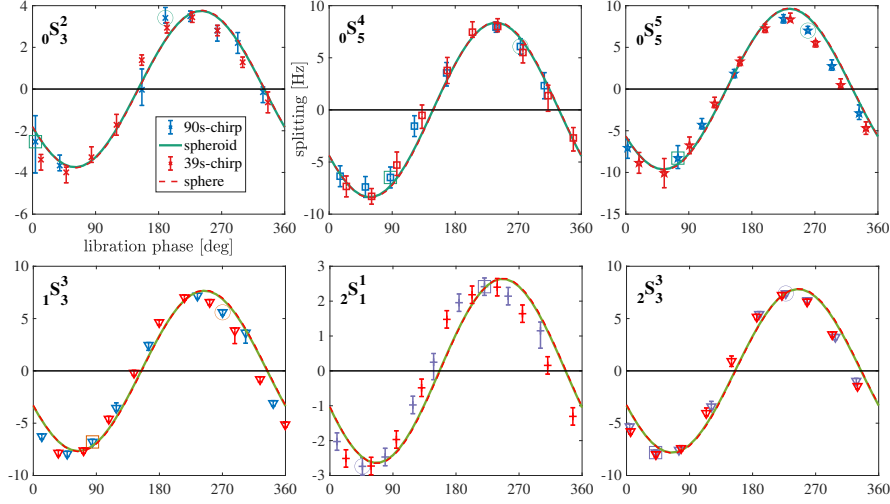


Fig. 6 Peak-to-peak frequency splitting $\delta f_{nS_l^{\pm m}}$ in Hz as a function of libration phase for six selected acoustic doublets $nS_l^{\pm m}$. Data points with error bars are measured in the ZoRo experiment librating with $f_o = 15$ Hz, $f_{lib} = 0.1$ Hz and $\Delta f = 1.5$ Hz. Phase-offset chirps with two different durations were used: 90s (blue) and 39s (red). Splittings predicted from Greenspan’s theory are drawn for ZoRo’s spheroid (solid line) and for the sphere (dashed line), which plot on top of each other.

computed at the rotation rate of the shell $f_{shell}(t)$, using the Ledoux coefficients of Vidal et al. (2020) computed for ZoRo’s flattening, but the difference with the spherical Ledoux coefficients is negligible except for the lowest frequency fundamental modes. The measurements are compared to the splittings predicted by the libration flow model for a spheroid (solid line) and for a sphere (dashed line), which are almost perfectly superposed. The signature of the time-varying libration flow is very well retrieved by MAV, but data appear to probe a libration flow that is about 20° further, which corresponds to a delay of about 0.5s. No significant difference is seen between the two chirp durations. We will get back to the delay problem in section 3.2.

Figure 7 compares two cases with different libration frequencies: $f_{lib} = 0.1$ Hz as in Fig. 6 versus $f_{lib} = 0.05$ Hz (98 s-long chirp). At smaller libration frequencies, fluid gets toward better synchronisation with shell’s rotation rate, implying smaller differential rotation and smaller phase shift between the fluid and the shell. This behaviour is clearly seen in the synthetic curves, and well recovered by MAV.

The splitting evolution with phase libration is shown in Appendix D for all 53 acoustic modes.

3.2 Short chirps results

We tested the short-chirp technique on acoustic doublet $1S_3^{\pm 3}$. First tests with chirps spanning 2350 to 2430 Hz in 4 seconds were performed for a uniform shell rotation, with f_o ranging from 1 to 20 Hz, providing splittings from 0.19 to 3.85 Hz, with error

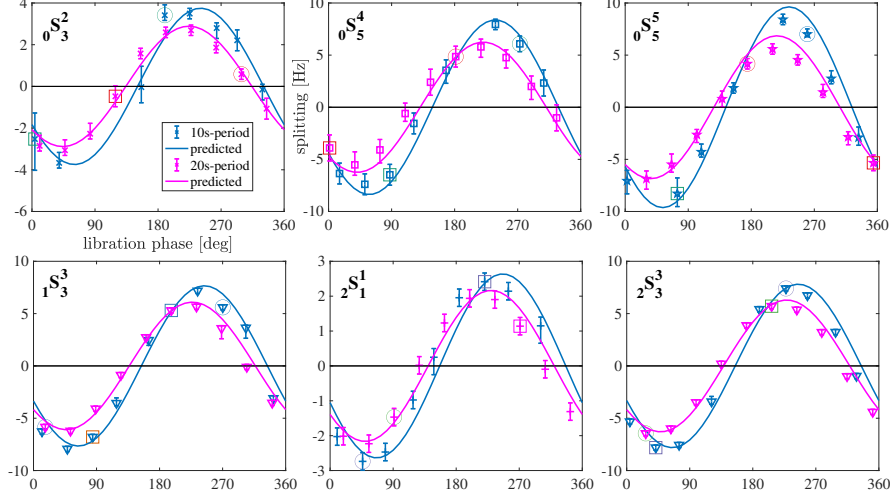


Fig. 7 Frequency splittings $\delta f_{nS_l^{\pm m}}$ for two different libration frequencies: $f_{lib} = 0.1$ Hz (blue) and 0.05 Hz (magenta), both with $f_o = 15$ Hz and $\Delta f = 1.5$ Hz as in Fig. 6. Symbols and error bars for measurements with 90s- and 98s-long phase-offset chirps. Sine solid lines for corresponding Greenspan’s predictions for ZoRo’s spheroid.

bars of about 0.01 Hz, in excellent agreement with Ledoux coefficients computed by 3^{rd} order-perturbation in ellipticity and rotation rate by Vidal et al. (2020).

The method was then applied to libration flows. Figure 8 shows an example of $1S_3^{\pm 3}$ doublet’s splitting as a function of libration phase. Libration parameters are $f_o = 15$ Hz, $f_{lib} = 0.084$ Hz and $\Delta f = 1.5$ Hz. A succession of 32 identical signals is played. Each signal consists of a 0.37 s-long chirp from 2360 to 2398 Hz, followed by a 0.37 s silence. The signal is played simultaneously by two loudspeakers placed at latitudes $+45^\circ$ and -45° along the same meridian, thus favoring equatorially symmetric modes. The overall sequence covers two libration periods. The resulting record is chopped to recover the response to each individual chirp, and the high-resolution algorithm is applied to each of the 32 extracted time records. The algorithm measures the probability for a given frequency to be present in the record. Figure 8 is a composite plot of the probability maps of all 32 segments. Two frequencies clearly emerge, which follow a sine pattern, thus revealing the variation of the $1S_3^{\pm 3}$ doublet’s frequency splitting as a function of libration phase. Note that the two sine curves cross each-other, because the splitting produced by the flow exceeds the Coriolis splitting for this doublet, as in Fig. 4.

We now go deeper into the analysis of these measurements. Figure 9 compiles several measurements and predictions for this doublet. We first retrieve the frequency splitting $\delta f_{nS_l^{\pm m}}$ for each chirp from the data of Fig. 8, yielding the green solid curve in Fig. 9. Note that the resulting sine curve is not centered on the zero line but on the magenta horizontal dash line, which marks the splitting due to solid body rotation at the f_o spin rate (*i.e.*, the Ledoux coefficient times f_o). The green dash-dot curve is a sine fit of the data obtained in another run, playing a succession of 64 chirps

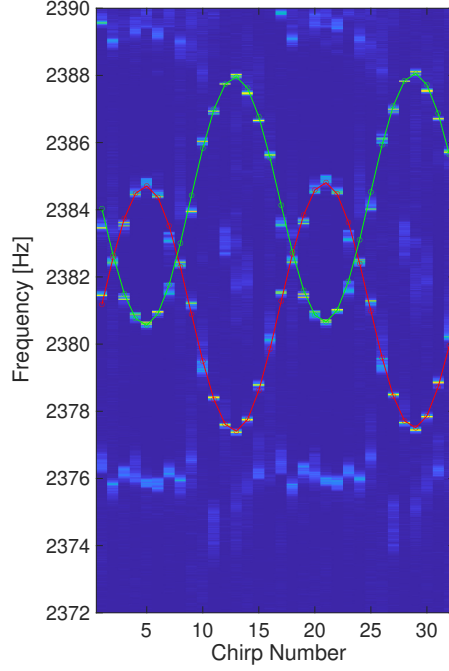


Fig. 8 Splitting example of the short chirps method. Libration parameters: $f_o = 15$ Hz, $f_{lib} = 0.084$ Hz and $\Delta f = 1.5$ Hz. A succession of 32 short chirps centered around the resonant frequencies of the $1S_3^{\pm 3}$ doublet. Each chirp plays frequencies 2360 to 2398 Hz in 0.37s and is followed by a silence of equal duration.

lasting 0.74s (no silence between chirps), from 2350 to 2430 Hz. The two curves almost coincide.

Let us compare these data with the splitting expected for this libration flow. The blue solid line gives the time-evolution of the frequency splitting predicted from Greenspan’s linear theory, after convolution of the time-dependent fluid flow with the acoustic kernel. The time taken into account for the computation of the flow is the center-time of the 0.74s-long chirp. The blue dotted line instead considers the start-time of the chirp, while the blue dash line considers the end-time of the chirp. We see that the data almost perfectly agree with the latter prediction, both in pattern, in amplitude, and in phase. We conclude that the mode splitting we measure is perfectly consistent with the fluid flow predicted by Greenspan’s linear theory. This is in line with the results shown in Fig. 2, which show an excellent agreement between that theory and a finite amplitude axisymmetric simulation. However, our measurements confirm a delay of the order of 0.3s between the flow and its acoustic modal response,

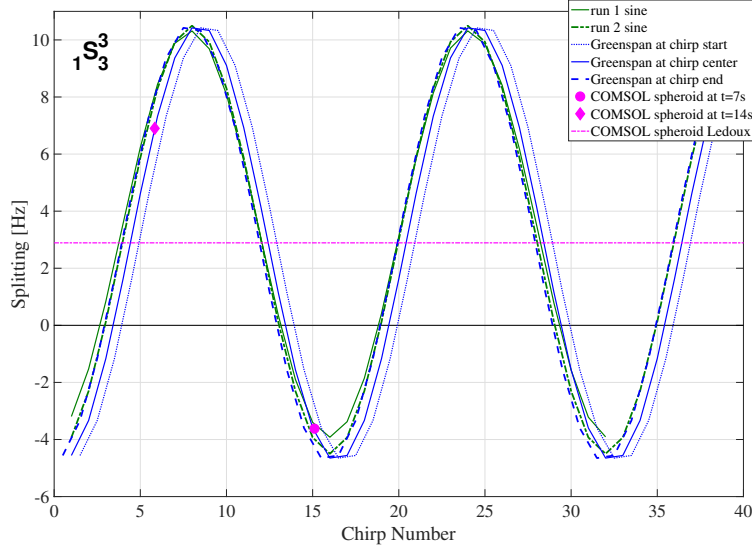


Fig. 9 Comparison between predicted and measured frequency splitting of the $1S_3^{\pm 3}$ doublet. Libration parameters as in Fig. 8: $f_o = 15$ Hz, $f_{lib} = 0.084$ Hz and $\Delta f = 1.5$ Hz. The x -axis is time given in chirp number. There are exactly 16 chirps in one libration period. The y -axis is the frequency difference between singlets $1S_3^{-3}$ and $1S_3^{+3}$. The green solid curve is derived from the data of Fig. 8. The green dash-dot line is the sine fit of frequencies obtained for another run (see text). The blue solid line gives the frequency splitting predicted by convolving Greenspan’s libration flow with the acoustic splitting kernel (for a sphere) of the $1S_3^{\pm 3}$ doublet. The blue dashed and blue dotted lines are the same prediction shifted by $-0.37s$ and $0.37s$ respectively. The magenta symbols are from a computation taking into account the exact spheroidal geometry of the experiment. The magenta horizontal dash line gives the splitting for solid body rotation at $f_o = 15$ Hz.

confirming the observations of section 3.1. We believe that it corresponds to the time for a mode to build up, as detailed in Appendix F.

We checked for another potential bias. The acoustic kernels we use to compute the predicted splittings are for a sphere. Since it was shown by Su et al. (2020) that theory had to be extended to second order perturbations in ellipticity in order to provide a correct ordering of the frequencies of a given multiplet, our simplification could introduce a bias. We checked that this was not the case, at least for the $1S_3^{\pm 3}$ doublet presented here. For that, we ran a simulation of the acoustic response of a ZoRo-like spheroid using the finite-element COMSOL Multiphysics® software, with $f_o = 15$ Hz, imposing Greenspan’s flow. The magenta symbols in Fig. 9 give the results we obtain for two different libration phases. They plot exactly on the blue solid line, which corresponds to the response of a sphere.

3.3 Acoustic mode splitting collection

Using the phase-shifted long chirp strategy, we were able to measure the splitting of 53 identified doublets, with frequencies between 500 and 5 000 Hz, from multiplet $0S_1$ to multiplets $0S_{14}$, $1S_{10}$, $2S_5$ and $3S_4$, for almost all libration phases.

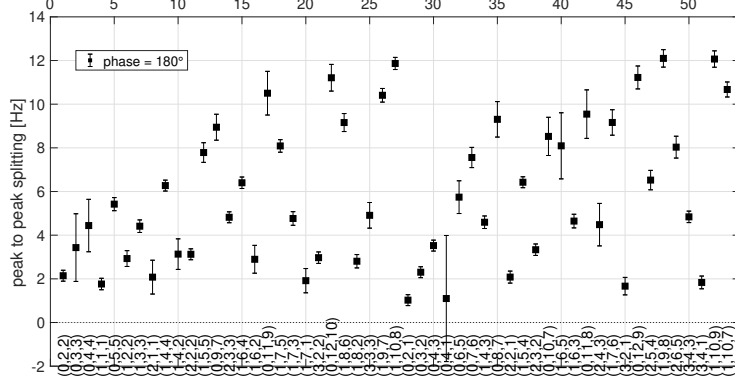


Fig. 10 Measured peak-to-peak splitting (in Hz) of 53 doublets, labeled along the x -axis by their $(n, l, |m|)$ index triplet. Libration-driven flow at a phase of 180° , with $f_o = 15$ Hz, $f_{lib} = 0.05$ Hz and $\Delta f = 1.5$ Hz.

Figure 10 shows an example of splittings measured for a libration phase of 180° (by least-square sine interpolation of the data at 10 libration phases), with $f_o = 15$ Hz, $f_{lib} = 0.05$ Hz and $\Delta f = 1.5$ Hz. Overtone ($n > 0$) spectral peaks are usually much more narrow than those of fundamentals ($n = 0$), yielding smaller splitting error bars. In the next sections, we invert these splittings to recover the time-evolution of the fluid flow, and evaluate the resolution power of these data.

4 Flow inversion

4.1 The SOLA inversion method

Given our splitting measurements of a collection of modes, we now want to invert these data and recover $f_{fluid}(t)$ at selected libration phases, using its relation with $\delta f_{n, S_l^{\pm m}}$ given by acoustic kernels ${}_n\mathbb{K}_l^m(s)$ (Eq. 11) or ${}_nK_l^m(r, \theta)$ (Eq. 5). Many inversion methods can be used for solving our linear problem. We will not review the vast literature on this topic, but only recall a few methods used in previous MAV studies. Two different methods were used in the seminal paper of [Triana et al. \(2014\)](#): a Tikhonov regularization and a semi-spectral Bayesian inversion. The former minimizes the second spatial derivatives of the flow velocity, while the latter relies on spherical harmonics to deal with the latitudinal flow variation, a Bayesian approach being taken for its radial variation. A critical assessment of both methods is given by [Mautino \(2016\)](#) who reviews several alternatives. He also stresses that, considering the limited number of modes used in these early studies, the choice of the model smoothness parameters plays a major role, a concern shared by [Su \(2020\)](#) who used the semi-spectral Bayesian algorithm.

In order to better assess the intrinsic resolving power of a given data set of acoustic splittings, it seems appropriate to turn to ‘Optimally Localized Averages’ (OLA) inversion methods, pioneered by [Backus and Gilbert \(1967\)](#). These methods have recently

gained a renewed interest in seismology (Zaroli 2019), and are widely used in helioseismology since the seminal papers of Pijpers and Thompson (1992, 1994). The idea of this class of methods is to extract from the data the best unbiased value of model parameters at a given location, or more precisely within a given volume around the target location. Two variants stand out: ‘Multiplicative Optimally Localized Averages’ (MOLA) and ‘Subtractive Optimally Localized Averages’ (SOLA).

The results of this article are obtained using the SOLA inversion method, closely following the detailed prescriptions of Zaroli (2019). Appendix G provides a summary of SOLA’s procedure and notations. In our 2D SOLA inversions, we target disks of a given radius in the meridional plane, while our targets are s -segments in our 1D inversions.

The main drawback of OLA inversion methods is that they only target a few selected spots of model space. Hence, they do not provide a complete continuous ‘best’ model. This prevents computing the resulting best fitting data, to be compared with the original data with their error bars. In the simple examples we show, we circumvent this limitation by targeting enough spots in model space. A smooth continuous model is then built by interpolation/extrapolation, from which synthetic data of the inverted model can be computed.

Although OLA methods are often presented as ‘parameter-free’, they involve a ‘trade-off’ parameter η , which governs the ratio between resolution misfit and model variance (see Eq. G7). The choice of η can be made to obtain a normalized misfit close to 1. Since we observe that Greenspan’s flow provides a very good fit to our splitting data, we can double check that the chosen ‘trade-off’ parameter provides flows that respect the smoothness of Greenspan’s flow, given the collection of mode splittings we retrieve, and the precision of the measurements.

Note that we aim at recovering the libration-induced flow rotation rate in the frame of the spinning shell. This is why we corrected measured frequency splittings from the Coriolis splitting computed for the instantaneous spin rate of the shell. We can then use the kernels presented in sections 1.2.3 and 1.2.2 to obtain f_{fluid} in the shell reference frame.

4.2 1D SOLA flow inversion

Since we do expect libration flow to be largely z -invariant, we start with 1D SOLA inversions. We obtained the frequency splitting of a collection of 53 acoustic doublets for 10 different phases of the periodic libration flow. Due to our acquisition strategy, the sampled libration phases are different for different modes. For all modes, the variation of the frequency splitting with libration phase is well fit by a sine. We thus use this sine pattern to interpolate our measurements to a set of 10 fixed libration phases from 0° to 324° in 36° steps. We attribute to each interpolated splitting an error equal to the mean of the 10 (or less) estimated errors for the considered measurements for each mode. An inversion of the 53 acoustic splittings is performed for each of the 10 selected libration phases. Note that although 10 independent inversions are computed, the data they invert correspond to the phases of a single sinusoidal fit of each mode.

4.2.1 Fluid rotation rate profiles

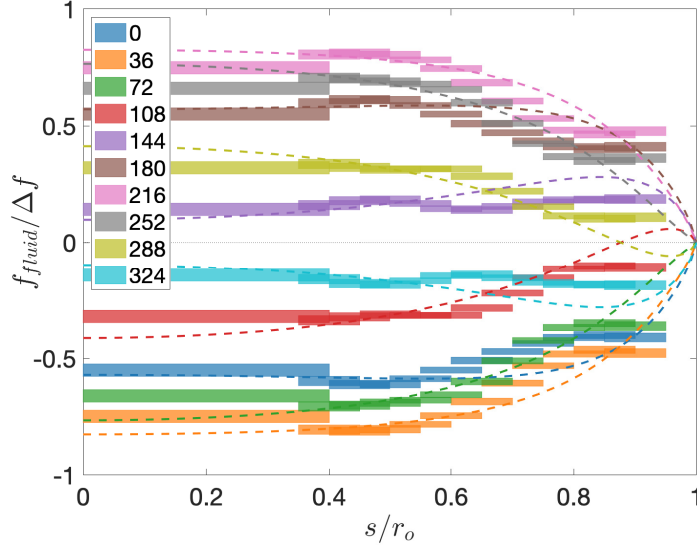


Fig. 11 1D SOLA inversion results for libration flow ($f_o = 15$ Hz, $f_{lib} = 0.05$ Hz and $\Delta f = 1.5$ Hz): normalized fluid rotation rate as a function of dimensionless cylindrical radius for 10 libration phases (legend in degrees). The width of the color boxes gives the targets' width, while their height is the inversion error. The color dashed lines are the predictions from Greenspan's flow at each libration phase delayed by 10° .

Figure 11 gathers the fluid rotation rate $f_{fluid}(s)$ s -profiles obtained from the inversions at 10 libration phases. The width of each box gives the target's width, while its height is the error estimate of the inverted model for this target. For comparison, we draw the profiles predicted by Greenspan's linear theory. We pointed out that the measured splittings appear to be late by a few tenths of a second, probably because our acquisition strategy does not account for the time it takes for an acoustic mode to build up. Therefore, we add a phase-delay of 10° (corresponding to 0.56s) to the synthetics.

For this inversion, we chose $\eta = 40$. The amplitudes and trends of the theoretical profiles are well retrieved in our inversion. However, the gentle decrease of f_{fluid} with s between $s/r_o = 0.7$ and $s/r_o = 1$ is not correctly retrieved. We will discuss the reasons for this disagreement in section 5, where we also explore the effect of different values of η .

4.2.2 Resolution kernels

An advantage of the SOLA inversion method is that it emphasizes the actual resolving power of the data, in a more objective way than other methods.

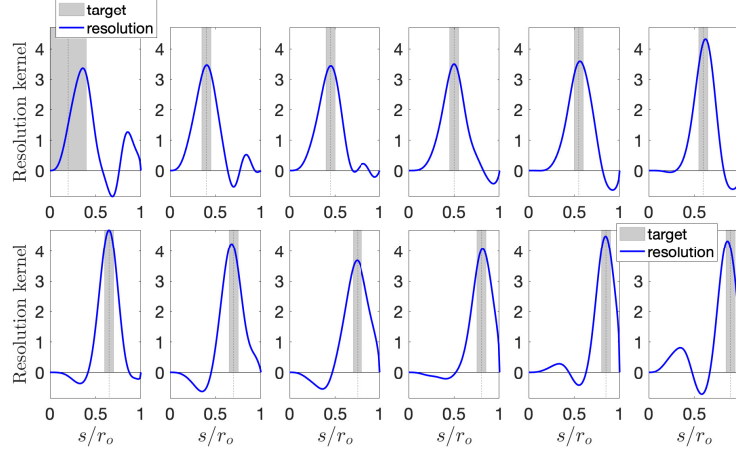


Fig. 12 Resolution kernels $A^{(k)}(s)$ for the 1D SOLA inversion of the splittings of 53 acoustic doublets. For each of the 12 targets, the resolution kernel is plotted as a function of dimensionless cylindrical radius, on top of a gray-shaded vertical band that gives the position and width of the target.

Figure 12 plots the resolution kernels $A^{(k)}(s)$ defined in Appendix G for the 12 s -segments we target. All resolution kernels appear well peaked around the target, except for the target near the center axis ($s/r_o = 0.4$). Low scores in these regions are expected, since all MAV flow kernels vanish on the axis (see Fig. 3). Negative lobes present for most kernels indicate that the estimate of the flow rotation rate we retrieve is not perfectly ‘unbiased’. We also note that the width of the resolution kernels at mid-height is at least twice as large as the targets’ width.

4.2.3 Data fits

We now examine the fit to the data achieved by our inverted 1D models. Remember that the SOLA method only provides the best model estimate at targets. We need a complete s -profile to compute the predicted frequency splittings of the acoustic doublets we inverted. We use MATLAB[®]’s modified Akima (Akima 1970) interpolation method to construct a smooth $f_{fluid}(s)$ curve, imposing $f_{fluid} = 0$ at $s/r_o = 1$. We can thus compare the measured frequency splittings, with their error bars, to the splittings predicted by our best model. Figure 13 shows such a comparison for a libration phase of 180° . We see that our model can explain almost all measurements within their error bars, with an average normalized misfit $misfit \simeq 0.73$, where $misfit$ is defined as:

$$misfit = \sqrt{\left\langle \left(\frac{\delta f_{pred} - \delta f_{meas}}{\sigma} \right)^2 \right\rangle}, \quad (12)$$

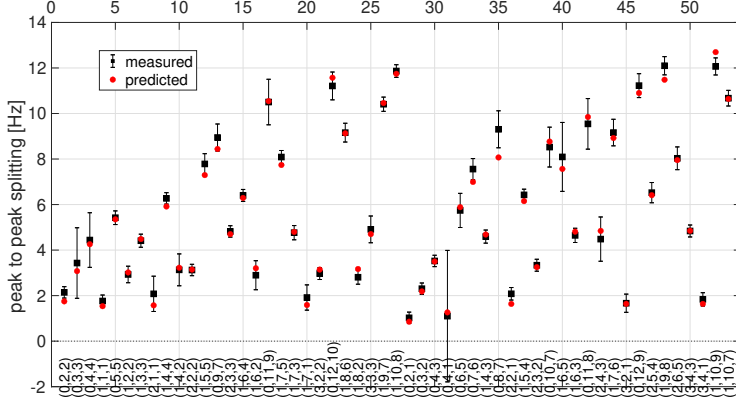


Fig. 13 Measured peak-to-peak frequency splitting of our collection of 53 acoustic doublets for a libration phase of 180° , with their error bars (black symbols). The red symbols are the splittings predicted from a smoothed s -profile of f_{fluid} of our inverted model (grey-shaded targets in Fig. 12). The $(n, l, |m|)$ indices of the modes are indicated beneath the x -axis.

in which δf_{meas} is the measured splitting of a given doublet, σ is its error bar, and δf_{pred} is the splitting predicted by the inverted model for the same mode. The average is performed over the 53 doublets of our collection.

4.3 2D SOLA flow inversion

We now turn to a 2D inversion, with the goal of examining how well our mode collection constrains the z -invariance of fluid flow that characterizes Greenspan’s asymptotic solution. We thus use the 2D kernels presented in section 1.2.2 to invert the same collection of 53 splittings and retrieve $f_{fluid}(r, \theta)$ at selected (r, θ) targets.

4.3.1 Fluid rotation rate maps

We chose 64 targets that cover most of an (r, θ) quarter-plane, as depicted in Fig. 14. Remember that one can only retrieve flows that are symmetrical with respect to the equator. Targets are placed on an (s, z) grid, so that we can draw smoothed s -profiles of f_{fluid} at different z , as depicted in Fig. 14c. The targets are disks, with radius equal to 0.025, except for the z -column at $s/r_o = 0.25$, where we chose a radius of 0.075, in anticipation of a poor spatial resolution near the axis.

Figure 14 displays the results we obtain for a libration phase of 180° , with $\eta = 40$. Inverted $f_{fluid}/\Delta f$ at target locations are given in 14a, with an error shown in Fig. 14b. Figure 14c gathers the s -profiles obtained at all 6 z -lines. Value for each target is given with a horizontal bar giving the target’s radius, and a vertical bar the estimated error. Smooth s -profiles computed as in section 4.2 are also drawn.

Figure 15 gathers the fluid rotation rate f_{fluid} s -profiles obtained from the inversions at 10 libration phases. The results are very similar to those shown in Fig. 12 from the 1D inversion. The 2D inversion confirms the z -invariance of the flow. The same deviations from Greenspan’s predictions show up for s/r_o between 0.7 and 1.

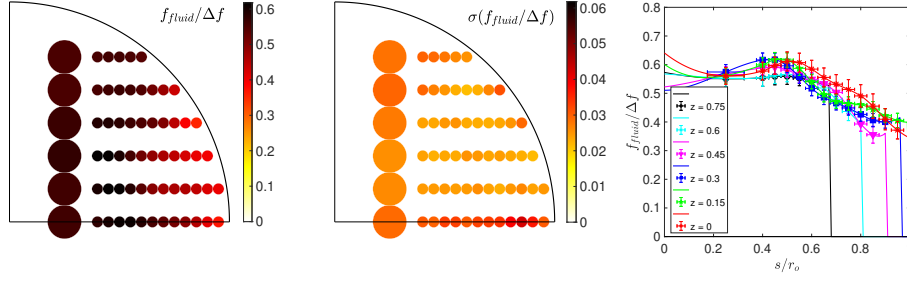


Fig. 14 2D SOLA inversion results for libration flow ($f_o = 15$ Hz, $f_{lib} = 0.05$ Hz and $\Delta f = 1.5$ Hz) at a libration phase of 180° . (a) disks in a meridional quarter-plane represent the location and size of the 64 chosen targets, and are colored with the value of the normalized fluid rotation rate $f_{fluid}/\Delta f$ obtained by the inversion. (b) the inversion error is colored in a similar representation. (c) $f_{fluid}/\Delta f$ as a function of cylindrical radius s for all 64 targets. At each target, the horizontal bar gives its width, while the vertical bar is the inversion error. Smoothed s -profiles (solid lines) are obtained from the targets' results at each of their 6 z -coordinate by modified Akima-interpolation.

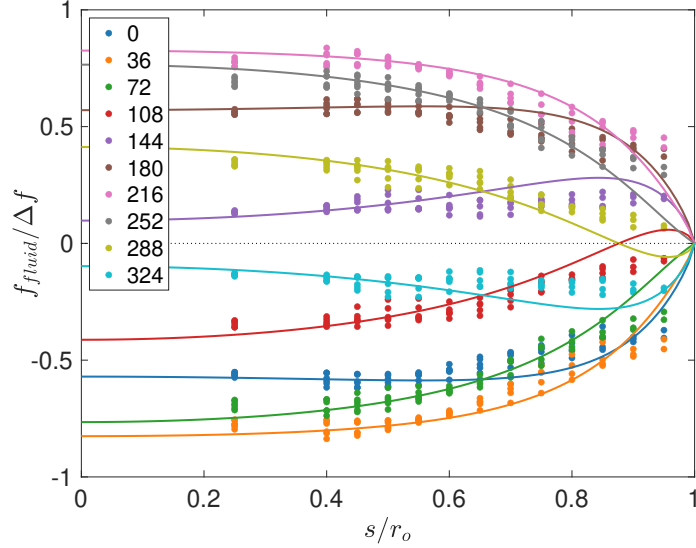


Fig. 15 2D SOLA inversion results for libration flow ($f_o = 15$ Hz, $f_{lib} = 0.05$ Hz and $\Delta f = 1.5$ Hz): normalized fluid rotation rate as a function of cylindrical radius for 10 libration phases (legend in degrees). For each libration phase, the values obtained at the 6 values of z are drawn. The color solid lines are the predictions from Greenspan's flow at each libration phase delayed by 10° .

4.3.2 Resolution kernels

Resolution kernels $A^{(k)}(r, \theta)$ are displayed in Fig. 16. As expected, resolution is very poor near the vertical axis. The kernels are rather well-peaked at target locations for most other targets, but their radius at mid-height is at least twice as large as the

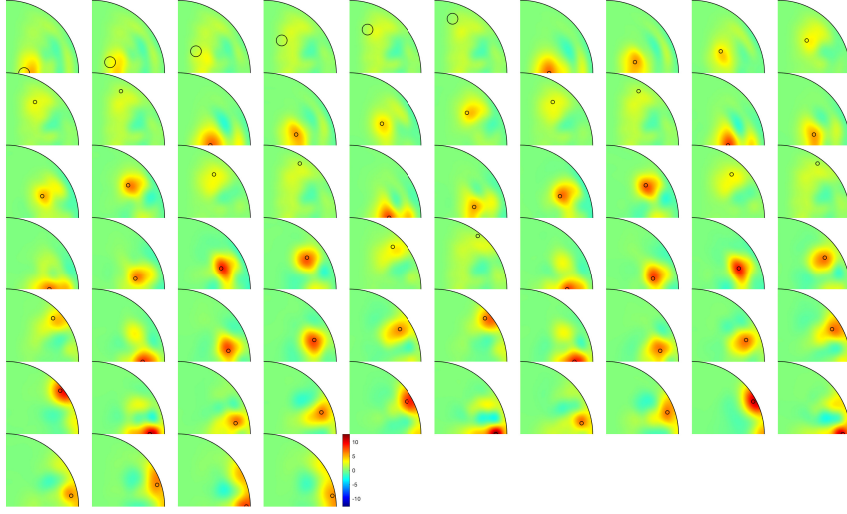


Fig. 16 Resolution kernels $A^{(k)}(r, \theta)$ for the 2D SOLA inversion of the splittings of 53 acoustic doublets. For each of the 64 targets, the amplitude of the resolution kernel is color-mapped in a meridional quarter-plane. A black circle indicates the position and radius of the target.

chosen target's radius, like in the 1D s -inversion. However, we observe that the 2D-inversion can clearly resolve the variation of flow rotation rate with z in most of the domain. We can thus be confident that the near-coincidence of the 6 s -profiles for each libration phase in Fig. 15 is a resolved feature of the flow, in agreement with Greenspan's theory.

4.3.3 Data fits

As discussed in section 4.2.3, we need a complete model in order to compute the predicted splittings. We thus constructed a smooth model by first interpolating the target's results along s (as shown in Fig. 14), and then interpolating these profiles in z . Both interpolations are performed with MATLAB®'s modified Akima (Akima 1970) interpolation. Fluid rotation rate is set to zero at the boundary ($r/r_o = 1$).

We can then compute the frequency splitting predicted by our inverted model for all 53 acoustic doublets. The fit to the data is almost identical to the fit of the 1D SOLA inversion shown in Fig. 13, with $misfit = 0.70$.

4.4 Trade-offs

Despite the excellent agreement between measured splittings and their prediction from Greenspan's flow model (apart for the observed time-delay), the retrieval of the fluid flow from these splittings appears somewhat disappointing. There is no problem with the time-variation, which is already established from the data and its sinusoidal fit.

However, one might have thought that the 1D s -inversion, with only 12 targets, would fit Greenspan’s profile. It is not quite the case, as shown in Fig. 12.

OLA inversion methods are often presented as ‘parameter-free’ (e.g. see Zaroli 2019). This is true in the sense that no a priori information on the model smoothness, for example, is needed. However, there remains a choice to be made on the trade-off parameter η . All results presented so far were obtained with $\eta = 40$, for both the 1D- and 2D-inversions.

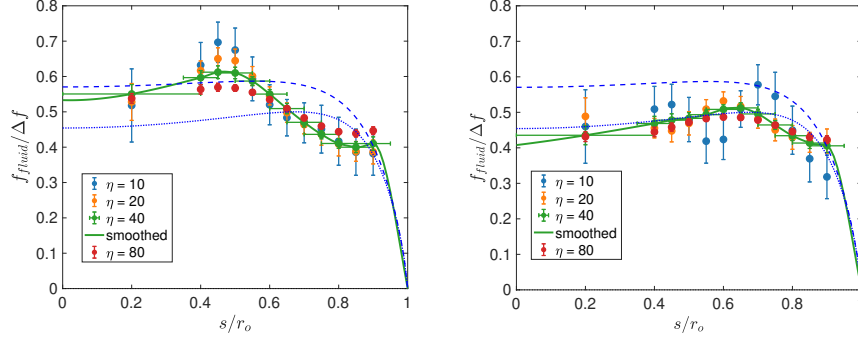


Fig. 17 Normalized fluid rotation rate as a function of cylindrical radius of target locations, from the inversion of frequency splittings at a 180° libration phase, for different values of the η parameter. The horizontal bars give the targets’ width, while the vertical bars are the inversion error. The blue dotted line is Greenspan’s profile at a libration phase of 180° , while the dashed blue line is the same at a phase delayed by 10° . (a) results from the inversions of measured splittings; (b) results from the inversions of synthetic splittings computed from Greenspan’s model.

In Fig. 17 we illustrate the impact of different choices for η , in the example of a 1D-inversion for a libration phase of 180° . Figure 17a compares the normalized fluid rotation rate obtained at our 12 s -targets for four inversions with values of η : 10, 20, 40 and 80. The smoothed profile is also shown for $\eta = 40$, together with Greenspan’s profiles for a libration phase of 180° (dotted line) and 190° (dashed line). We observe that all models overestimate fluid velocity around $s/r_o = 0.5$, and underestimate it between $s/r_o = 0.6$ and 0.9 . This is a consequence of the trade-offs between these two regions, which is also visible in the side lobes of the resolution kernels shown in Fig. 12. Increasing η reduces the oscillation and widens the resolution kernels. It also reduces the error on the inverted model, but this error only measures the propagation of the data error in the ‘weighted average’ (Zaroli 2019). It does not reflect the deviation of that weighted average from the true model. The average normalized misfit only weakly depends upon η , with $misfit = 0.73, 0.74, 0.73$ and 0.83 for $\eta = 10, 20, 40$ and 80 , respectively.

Deviations of the inverted models from Greenspan’s flow model could be due to the ellipticity of the ZoRo shell, which is not taken into account in our sensitivity kernels. It could also be the sign of flow complexities that show up for strong enough libration (Noir et al. 2009). They could also be due to limitations of the acquisition strategies, or to a variation of the observed time-delay with mode numbers. We don’t think that it is the case, because of the excellent agreement between observed splittings and those

predicted by convolving Greenspan’s flow with the acoustic sensitivity kernels, and also because synthetic tests display similar spurious oscillations. This is illustrated in Fig. 17b, which shows profiles obtained from the inversions of synthetic splittings, predicted by Greenspan’s flow model, using the same collection of modes, with their individual error, and adding a random noise within that error range. Oscillations around the true model (dotted blue line) are observed for the different values of η . The reason is to be found in the limited spatial resolution allowed by the set of 53 splittings we could measure. Figure 3 shows that individual sensitivity kernels are a bit wide, and that their complementarity is limited.

5 Limitations and perspectives

To date, Modal Acoustic Velocimetry has been primarily utilized for mapping fluid flows in gas-filled containers under steady or statistically steady conditions (Triana et al. 2014; Mautino 2016; Su et al. 2020; Su 2020). This study introduces and evaluates two distinct strategies for acquiring acoustic data in environments with non-stationary gas flows.

The first strategy is applicable to time-periodic flows. By employing a series of long chirps, each offset by an increasing phase lag relative to the periodic flow, we can extract the frequency splitting of a substantial collection of acoustic doublets (typically 60) from each spectrum in the series. This approach allows us to sample the flow at various phases, resulting in a comprehensive flow map upon inversion, thanks to the large number of recovered doublets.

The second strategy involves using a sequence of very short chirps that can track the evolution of the flow. This method is suitable for monitoring non-periodic flows, albeit with limited information derived from a small number of acoustic doublets (typically 1 to 4). The high-resolution algorithm developed for this strategy offers a significantly higher resolution of frequency splitting compared to classical measurements from power spectra.

Conversely, the short chirp strategy offers limited flow information. Preliminary tests combining both strategies have proven effective in enhancing precision, particularly when the number of intervening frequencies is limited. However, this combined approach is less successful when multiple modes are present within the considered time window. Further refinement of this combined strategy could potentially yield better results.

Both strategies have revealed a time delay of a few tenths of a second between when an acoustic mode’s eigenfrequency is played and when it samples the flow. This delay is likely due to the time required for a mode to build up, a phenomenon that warrants further analysis. Libration-induced flows offer a unique unexpected tool for investigating the buildup process of a large collection of acoustic modes.

Although data acquisition is relatively fast, post-processing is time-consuming, requiring visual inspection of spectra for reliable mode identification and splitting measurement. Currently, we lack splitting measurements for ${}_nS_l^{\pm m}$ doublets with $m \lesssim l$ due to overlapping spectral peaks with neighboring doublets. For fundamental doublets ($n = 0$), spectral peaks are wide and often ambiguous. However, synthetic

spectra computed for Greenspan’s flow model fit these unresolved spectra well, indicating the feasibility of extracting more information from the full frequency spectrum or time-domain analysis. This suggests the potential for more automated or artificial intelligence-based processing in the future.

Concerning the inversion, the use of spherical sensitivity kernels is an approximation that is acceptable given the current data precision, but spheroidal sensitivity kernels (Albo et al. 2010) should be used as data improves.

6 Conclusion

We present measurements of libration-induced flows in a rapidly spinning gas-filled spheroid. Such experiments are key for exploring the dynamics of rapidly spinning bodies, such as stars or planetary cores. The strong centrifugal acceleration prevents the use of classical PIV techniques, calling for a particle-free method. This led us to adapt the recently proposed Modal Acoustic Velocimetry method (Triana et al. 2014) to time-varying fluid flows, for which we imagined and tested two acquisition strategies.

The first strategy involves exciting a large collection of acoustic modes by playing long-duration chirps (typically 100s) spanning a large frequency range (typically from 500 to 5 000 Hz) in order to obtain a good spectral resolution (typically 0.01 Hz) of the resonance peaks, and thus of the frequency splitting produced by the flow. By playing such chirps several times (typically 10 times) starting at successive phases of the libration-induced flow, we can recover the time-evolution of the flow. The key is to relate the time at which a given acoustic doublet is excited to the libration phase at that instant.

The second strategy targets individual acoustic doublets, which we excite by a succession of short chirps (typically spanning 80 Hz in 0.4s). Each chirp probes a different phase of libration. For such a short chirp, a standard power spectrum is not efficient at resolving the frequency splitting of the doublet. However, its duration is long enough for hundreds of cycles to be played and recorded. We thus apply a high-resolution algorithm that tests for the presence of a limited number of monochromatic components and yields the two dominant frequencies, corresponding to the individual singlets.

Both methods yield mode splittings that agree very well with the predictions derived from Greenspan’s linear theory (see Fig. 6-9 and Fig. D4-D5). However, we observe a small unexpected delay, which we attribute to the time needed for the acoustic mode to build up. A detailed study of this delay could bring interesting constraints to this buildup process.

We then applied the SOLA inversion method to a set of 53 frequency splittings of acoustic doublets, acquired for several phases of a libration-driven flow. The inversion yields the fluid flow rotation rate f_{fluid} as a function of cylindrical radius s (1D-inversion) or in an (r, θ) meridional quarter-plane (2D-inversion). The retrieved values, shown in Fig. 11 and 15, respectively, are in good agreement with Greenspan’s solution for this libration flow. The flow amplitudes and time-variation are very well retrieved, but the exact s -profiles of f_{fluid} are not perfectly recovered. The analysis of the resolution kernels, shown in Figs 12 and 16, indicates that the data offer a

good (r, θ) -resolution, but over an averaging area of approximately 5% of a meridional quarter-plane. The resolution vanishes near the vertical spin axis, and some trade-offs are present, particularly in the equatorial region.

Our study paves the way for broader experimental studies of libration or precession flows in more exotic regimes.

Supplementary information. Supplementary Material provides the audio file example HP0111_per_spe_O15L3T12.3f.wav (30.8 Mo). The file is in the ‘WAV’ format and contains 11 channels sampled at 44100 Hz on 16 bits. The first eight channels are the signals recorded by 8 microphones situated at a latitude of $\pm 32^\circ$ and different longitudes. Channels 9 and 10 record a libration trigger signal, and a chirp start signal, respectively. Channel 11 records a magnetometer signal used as a rev-counter (see Appendix C for details). The file contains the acoustic response of the ZoRo experiment to a succession of 32 short signals simultaneously played on two loudspeakers at latitudes $+45^\circ$ and -45° along the same meridian. Each of the 32 signals consists in a short chirp, playing frequencies 2360 to 2398 Hz in 0.37s, followed by a silence of equal duration. This chirp targets acoustic doublet ${}_1S_3^{\pm 3}$. Libration parameters are: $f_o = 15$ Hz, $f_{lib} = 0.0841$ Hz, and $\Delta f = 1.5$ Hz.

Acknowledgments. HCN thanks Christophe Zaroli for useful comments on the SOLA inversion method. This work was partly supported by the Programme National de Planétologie (PNP) of CNRS-INSU co-funded by CNES. DC received funding from the ERC under the European Union’s Horizon 2020 research and innovation program via the THEIA project (grant agreement no. 847433). ISTerre is part of Labex OSUG@2020 (ANR10 LABX56).

Declarations

Some journals require declarations to be submitted in a standardised format. Please check the Instructions for Authors of the journal to which you are submitting to see if you need to complete this section. If yes, your manuscript must contain the following sections under the heading ‘Declarations’:

- Funding This work was partly supported by the Programme National de Planétologie (PNP) of CNRS-INSU co-funded by CNES. DC received funding from the ERC under the European Union’s Horizon 2020 research and innovation program via the THEIA project (grant agreement no. 847433). ISTerre is part of Labex OSUG@2020 (ANR10 LABX56).
- Conflict of interest/Competing interests (check journal-specific guidelines for which heading to use) The authors declare no conflict of interest.
- Ethics approval Not applicable.
- Consent to participate
- Consent for publication
- Availability of data and materials
- Code availability
- Authors’ contributions The improvements of the ZoRo set-up for this study were conducted by PC, SS, YD and HCN. PR proposed and performed the high-resolution

analysis. DC provided Greenspan’s flow solution for the spheroid and performed the COMSOL simulations. HCN proposed the long-chirp strategy, performed the runs and their processing. SS guided the use of the SOLA inversion method. HCN performed the inversions and their analysis. This article was written by HCN, with complements and review by all authors.

If any of the sections are not relevant to your manuscript, please include the heading and write ‘Not applicable’ for that section.

Editorial Policies for:

Springer journals and proceedings: <https://www.springer.com/gp/editorial-policies>

Appendix A Libration in a spheroid

Given a longitudinal libration of the spheroid given by Eq. 1, we derive the expression of the fluid rotation rate $f_{fluid}(s, t)$ in the reference frame of the spinning spheroid. The spheroid being specified by its equatorial r_{eq} and polar r_{pol} radii, we define

$$\frac{f_{Ekman}}{f_o} = \sqrt{\frac{\nu}{2\pi f_o r_{eq}^2}} = Ek^{1/2} \quad \text{and} \quad c = \frac{r_{pol}}{r_{eq}}.$$

The regime of interest is $f_{lib}/f_o \ll 1$ in our case, and the boundary Ekman layers can then be considered as steady. Greenspan and co-workers (Greenspan and Howard 1963; Greenspan 1968) have studied the spin-up of a fluid in axisymmetric containers of geometry $-g(s) \leq z \leq h(s)$. Using equation (5.17) of Greenspan and Howard (1963), we obtain that the expression for $f_{fluid}(s, t)$ is the same as Eq. 2 for the sphere if the ξ parameter is given by

$$\xi = \frac{f_{lib}}{f_{Ekman}} \frac{g + h}{[1 + (g')^2]^{1/4} + [1 + (h')^2]^{1/4}}, \quad (\text{A1})$$

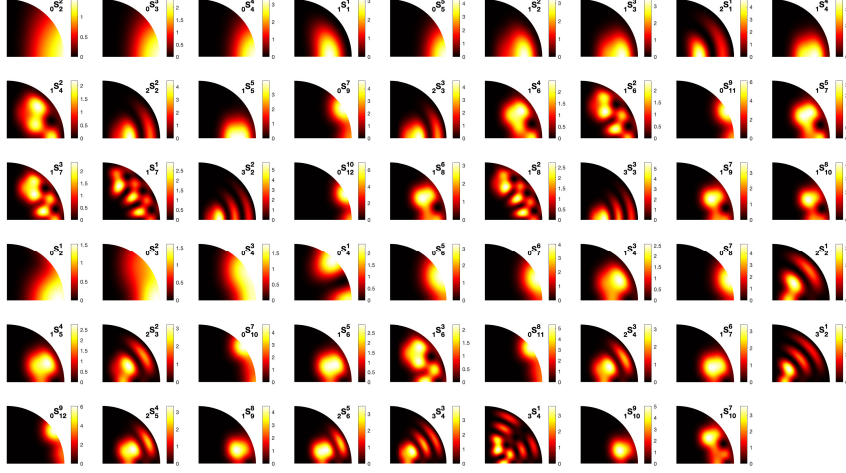
where the prime denotes the derivative with respect to the cylindrical radius s . Considering the spheroid geometry $g = h = c(1 - s^2)^{1/2}$, we retrieve that ξ^{-1} is given by equation (A10) of Noir and Cébron (2013), *i.e.*

$$\xi = \frac{f_{lib}}{f_{Ekman}} \frac{h^{3/2}}{(h^2 + c^4 s^2)^{1/4}} = \frac{f_{lib}}{f_{Ekman}} \frac{c}{[1 - s^2(1 - c^2)]^{1/4}} (1 - s^2)^{3/4}, \quad (\text{A2})$$

where the cylindrical radius s is now normalized by r_{eq} . Since $1 + (h')^2 = h^{-2}$ in the sphere ($c = 1$), ξ is easily formulated in function of the normalized semi-column height $h(s)$. By contrast, Eq. A2 cannot be simply derived from the formula in the sphere (Eq. 2) where the normalized semi-column height h in the sphere would have been replaced by that of the spheroid $h = c(1 - s^2)^{1/2}$. Note finally that the fluid response $f_{fluid}(s, t)$ can also be obtained for any values of f_{lib}/f_o by considering time periodic boundary layers, but at the price of a more complex expression (Cébron et al. 2021).

Appendix B 2D sensitivity kernels

Figure B1 shows the 2D sensitivity kernels ${}_nK_l^m(r, \theta)$ for the collection of 53 acoustic doublets ${}_nS_l^{\pm m}$ inverted in this study. The ellipticity of ZoRo's shell is ignored for these kernels.



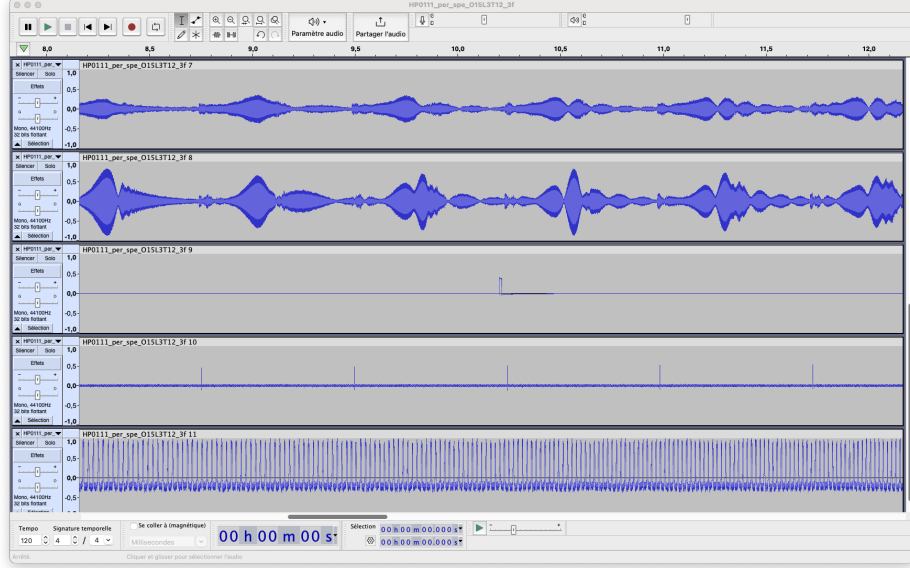


Fig. C2 Audacity®screenshot of part of a typical audio file. Only channels 7 to 11 are shown. Channels 7 and 8 are microphone records. Channel 9 shows one libration nul-phase trigger. Five chirp start triggers are seen on channel 10. Channel 11 records the magnetometer signal that is used as a rev-counter.

stems mark times at which the libration phase is an integer multiple of 2π , as read from channel 9. The red vertical stems mark chirp starts obtained from channel 10. The blue dots give the instantaneous spin rate of the spheroid computed from the magnetometer signal of channel 11. It can be compared with the requested spin rate (green line) constructed from the libration parameters ($f_o = 15$ Hz, $f_{lib} = 0.084114$ Hz, $\Delta f = 1.5$ Hz) timed by channel 9's trigger.

For this to work, the motor drive should execute the instructions with a minimal delay. The Kollmorgen AKM73Q® motor drive executes instructions sent by a National Instruments real-time compactRIO (cRIO) controller via an EtherCAT® network communication protocol. The requested motor spin rate, and the measured torque and spin rate are exchanged between the cRIO and the servo every 1ms (larger than the $62.5\mu s$ lower limit for this protocol). The measured values are averaged over 10 samples. The whole experiment is controlled by a home-made program, written in National Instrument LabVIEW® language, and operated through a multi-tabs user interface running on a Windows® Personal Computer (PC) connected to the cRIO via ethernet. All other measurements are retrieved through Data Acquisition Cards connected to this PC.

The PID settings of the motor drive result from a compromise: minimize the time-delay between instructed and achieved spin rate, while keeping the level of instantaneous torque fluctuations low enough to limit noise and allow for large libration amplitudes.

Our acoustic chirps are computed by a Python program and written in a six channels WAV file. The first four channels are the signals sent to each of the four

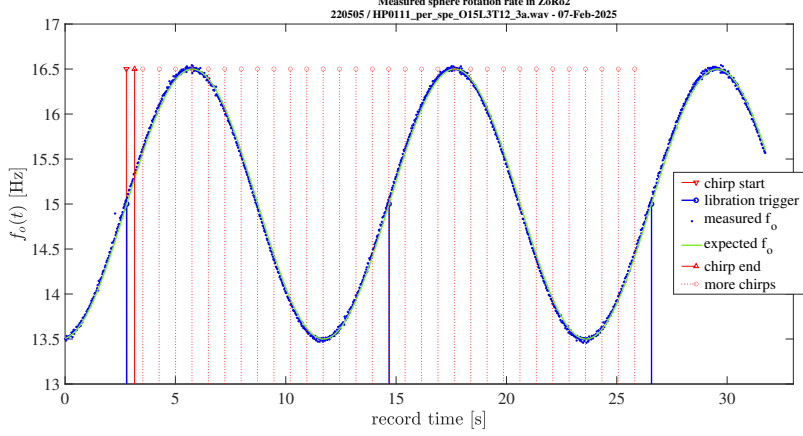


Fig. C3 Example of libration diagnostics. Instantaneous spinning rate of the spheroid as a function of time. The blue vertical stems mark times at which the libration phase is an integer multiple of 2π . The red vertical stems mark chirp starts. The blue dots give the instantaneous spin rate of the spheroid computed from the magnetometer signal. It can be compared with the requested spin rate (green line) constructed from the libration parameters ($f_o = 15$ Hz, $f_{lib} = 0.084114$ Hz, $\Delta f = 1.5$ Hz). \mathfrak{I}

loudspeakers, while the last two only contain a trigger that marks the chirp start. All six channels are played by an ASUS®Xonar DGX audio card in the main PC. Tests reveal that the signals sent by the audio card are delayed by 15ms on channels O5 and O6, and by 5ms on channel O4. These delays are corrected for in the synchronization software. We checked that no delay was introduced on all channels of the TASCAM®US-16x8 Audio/MIDI Interface used to process the microphone signals.

Appendix D Additional frequency splitting plots

Figures D4 and D5 show frequency splitting versus libration phase for our collection of 53 acoustic doublets ${}_nS_l^{\pm m}$. ZoRo is filled with nitrogen at atmospheric pressure. Libration parameters are: $f_o = 15$ Hz, $f_{lib} = 0.05$ Hz and $\Delta f = 1.5$ Hz. Chirps played from 500 to 5000 Hz in 82s. Measured splittings are plotted with their error bars. The dashed lines are sine-interpolations of the measurements. The solid lines are predictions obtained by convolving the geostrophic azimuthal flow of Greenspan's theory with the splitting kernel of each acoustic doublet.

Appendix E High-resolution algorithm

Many theoretical, numerical, and experimental works have been performed on the determination of discrete frequencies in a multi-tone audible signal that can be generalized to a complex spectrum search (Kay and Marple 1981). High-resolution methods were developed such as the multiple signal classification (MUSIC) technique (Rajan and Bhatta 1993; Candy and Sullivan 1989; Chouhan and Anand 1993; Krasny and Antonyuk 1997), the Prony method (Shang et al. 1988), and the more sophisticated

ESPRIT algorithm (Roy and Kailath 1989; Roy et al. 2003). This latter approach is similar to the more general matrix-pencil method (Hua and Sarkar 1990; Laroche 1993).

The originality of IRWIN (Roux et al. 2004; Philippe et al. 2008) is to combine a modified Prony method (Scharf and Demeure 1991) with an iterative approach that looks for the frequency occurrence when different sets of data points are chosen within the time record.

We present here the main steps of the algorithm. We assume that the acoustic pressure field recorded at a given microphone is dominated by M monochromatic signals. Naming δt the sampling time step of the record, we can express the time-record $P(n)$ over a time-window $n\delta t$ as:

$$P(n) = \sum_{m=1}^M \tilde{a}_m [\exp(i\omega_m \delta t)]^n = \sum_{m=1}^M \tilde{a}_m z_m^n, \quad (\text{E3})$$

where ω_m is the angular frequency of the m monochromatic component, and \tilde{a}_m its amplitude. Our goal is to identify the components z_m of largest amplitude from a collection of time-windows with increasing number of points n , *i.e.* solving the following set of equations:

$$\begin{cases} P(0) &= \tilde{a}_1 + \tilde{a}_2 + \dots + \tilde{a}_M \\ P(1) &= \tilde{a}_1 z_1 + \tilde{a}_2 z_2 + \dots + \tilde{a}_M z_M \\ \dots & \\ P(M-1) &= \tilde{a}_1 z_1^{M-1} + \tilde{a}_2 z_2^{M-1} + \dots + \tilde{a}_M z_M^{M-1} \\ \dots & \\ P(2M-1) &= \tilde{a}_1 z_1^{2M-1} + \tilde{a}_2 z_2^{2M-1} + \dots + \tilde{a}_M z_M^{2M-1} \end{cases} \quad (\text{E4})$$

The first step is to symbolically invert the first M equations of this system to express amplitudes \tilde{a}_1 to \tilde{a}_M as a function of the data $P(0)$ to $P(M-1)$ and of the phases z_1 to z_M . Replacing \tilde{a}_1 to \tilde{a}_M in the last M equations, one obtains a system that is strongly non-linear in the variables z_m but linear in the Elementary Symmetric Polynomials (*ESP*) E_m of the z_m unknowns, given by:

$$E_1 = \sum_{i=1}^M z_i, E_2 = \sum_{i=1}^M \sum_{j=i+1}^M z_i z_j, \dots, E_M = \pi_{i=1}^M z_i. \quad (\text{E5})$$

One thus recovers the following set of linear equations:

$$\begin{cases} P(M) &= P(M-1)E_1 - P(M-2)E_2 + \dots + (-1)^{M-1}P(0)E_M \\ P(M+1) &= P(M)E_1 - P(M-1)E_2 + \dots + (-1)^{M-1}P(1)E_M \\ \dots & \\ P(2M-1) &= P(2M-2)E_1 - P(2M-3)E_2 + \dots + (-1)^{M-1}P(M-1)E_M \end{cases} \quad (\text{E6})$$

The *ESP* are then easily obtained. The unknowns z_m are obtained as the roots of a polynomial of degree M whose coefficients are the *ESP* E_1 to E_M .

Appendix F Acoustic mode buildup

Both strategies we developed rely on the capture of the flow by a given acoustic mode. When the flow is time-dependent, the question is: when does the mode capture the flow? The results presented in sections 3.1 and 3.2 both indicate that this capture occurs a few tenths of a second after the resonance peak frequency of the mode is played. Here, we show that this is comparable to the time it takes for a mode to build up or to fade away.

We tested mode buildup by first identifying the resonant frequency of a few modes, playing 10s-long monochromatic sounds, with a step-by-step frequency increase of 1 Hz. The frequency yielding the largest amplitude is the resonant frequency. We then played a sine signal at this frequency for 10s, and observed the raise of the response on our microphone array.

Figure F6 shows the growth and decay of mode ${}_1S_3^3$ at one microphone. The envelope of the signals can be fit by $1 - \exp(-t/\tau)$ and $\exp(-t/\tau)$ functions (Trusler 1991, p.219), defining buildup time τ . In the ZoRo experiment at rest, our measurements yield buildup times $\tau = 0.30, 0.22$, and 0.20 s for modes ${}_0S_2^2$, ${}_1S_3^3$ and ${}_2S_1^0$, respectively. We have not conducted a systematic survey of these buildup times, and the effect of the rotation, of playing a chirp, and of the convolution with the time-varying flow remain to be explored. However, this analysis supports our interpretation of the observed time-delay of our observation with respect to Greenspan’s prediction as being due to mode buildup.

Appendix G SOLA inversion

We recall here the SOLA algorithm, closely following the rules and notations given by Zaroли (2019). The SOLA method aims at finding the *optimal unbiased weighted average* $\hat{m}^{(k)}$ of the true model $m(\mathbf{r})$ over a given target k , defined by a function $T^{(k)}(\mathbf{r})$, typically a ball centered on $\mathbf{r}^{(k)}$. For that, it minimizes a cost function:

$$\mathcal{C}^{(k)} = \int \left[A^{(k)}(\mathbf{r}) - T^{(k)}(\mathbf{r}) \right]^2 d^3\mathbf{r} + \eta^2 \sigma_{\hat{m}^{(k)}}^2 \quad (\text{G7})$$

subject to the *unimodular condition*:

$$\int A^{(k)}(\mathbf{r}) d^3\mathbf{r} = 1. \quad (\text{G8})$$

The first term of $\mathcal{C}^{(k)}$ measures the deviation of the *averaging kernel* from the target kernel, while the second term measures the model variance, weighted by the square of the trade-off parameter η . Note that, following Zaroли (2019), we choose the same value of η for all targets k .

Because of the linear relationship between the model parameters and the measured data, one can express the optimal model we are looking for as:

$$\hat{m}^{(k)} = \sum_{i=1}^N x_i^{(k)} d_i, \quad (\text{G9})$$

with N the number of measurements d_i . The inversion consists in finding the coefficients $x_i^{(k)}$ that minimize the cost function $\mathcal{C}^{(k)}$. One can then recover the weighted average $\hat{m}^{(k)}$ from Eq. G9, and the averaging kernel (resolution kernel) by:

$$A^{(k)}(\mathbf{r}) = \sum_{i=1}^N x_i^{(k)} K_i(\mathbf{r}), \quad (\text{G10})$$

where $K_i(\mathbf{r})$ is the sensitivity kernel of the i^{th} data. The propagated model error is obtained from:

$$\sigma_{\hat{m}^{(k)}}^2 = \sum_{i=1}^N \left(x_i^{(k)} \right)^2. \quad (\text{G11})$$

Note that $\sigma_{\hat{m}^{(k)}}$ only measures the error brought by propagating the data errors to the model space. It is not an estimate of the ‘true’ error, as defined as the weighted average $\hat{m}^{(k)}$ estimate minus the ‘true’ model $m(\mathbf{r}^{(k)})$.

We refer the reader to section 2 of Zaroli (2019) for a detailed description of the SOLA inversion procedure that yields the requested $x_i^{(k)}$ coefficients.

In our application, the data vector d_i is the set of peak-to-peak frequency splittings, corrected for the Coriolis splitting of the spinning shell, and normalized by their measurement error. The weighted average $\hat{m}^{(k)}$ is the inverted rotation rate f_{fluid} of the fluid flow in the spinning shell reference frame, at a given target k . The target function $T(\mathbf{r})^{(k)}$ is defined on an s -segment between $s^{(k)} - w^{(k)}$ and $s^{(k)} + w^{(k)}$ in the 1D-inversion, and on a disk of radius $w^{(k)}$ centered on an $(r, \theta)^{(k)}$ point in the 2D-inversion. In both cases, its uniform amplitude $a^{(k)}$ is set in order for $T(\mathbf{r})^{(k)}$ to satisfy the unimodular condition (Eq. G8).

References

- Aerts, C., Christensen-Dalsgaard, J., Kurtz, D.W.: Asteroseismology. Springer, Dordrecht Heidelberg London New York (2010)
- Albo, P.G., Gavioso, R., Benedetto, G.: Modeling steady acoustic fields bounded in cavities with geometrical imperfections. *International Journal of Thermophysics* **31**(7), 1248–1258 (2010)
- Akima, H.: A new method of interpolation and smooth curve fitting based on local procedures. *Journal of the ACM* **17**(4), 589–602 (1970)
- Aldridge, K.D.: An experimental study of axisymmetric inertial oscillations of a rotating liquid sphere. PhD thesis, Massachusetts Institute of Technology (1967)

- Adrian, R.J., Westerweel, J.: Particle Image Velocimetry vol. 30. Cambridge university press, ??? (2011)
- Brito, D., Alboussière, T., Cardin, P., Gagnière, N., Jault, D., La Rizza, P., Masson, J.-P., Nataf, H.-C., Schmitt, D.: Zonal shear and super-rotation in a magnetized spherical Couette-flow experiment. *Phys. Rev. E* **83**(6, Part 2), 066310 (2011) <https://doi.org/10.1103/PhysRevE.83.06631>
- Backus, G.E., Gilbert, J.: Numerical applications of a formalism for geophysical inverse problems. *Geophysical Journal International* **13**(1-3), 247–276 (1967)
- Burmann, F., Noir, J., Beetschen, S., Jackson, A.: Low-cost solutions for velocimetry in rotating and opaque fluid experiments using ultrasonic time of flight. *Experimental Techniques* **46**(3), 429–439 (2022)
- Brito, D., Nataf, H.-C., Cardin, P., Aubert, J., Masson, J.-P.: Ultrasonic Doppler velocimetry in liquid gallium. *Exp. Fluids* **31**, 653–663 (2001)
- Busse, F.H.: Mean zonal flows generated by librations of a rotating spherical cavity. *Journal of Fluid Mechanics* **650**, 505–512 (2010)
- Chouhan, H.M., Anand, G.: Normal mode wave-number estimation using a towed array. *The Journal of the Acoustical Society of America* **93**(4), 1807–1814 (1993)
- Comstock, R.L., Bills, B.G.: A solar system survey of forced librations in longitude. *Journal of Geophysical Research: Planets* **108**(E9) (2003)
- Candy, J.V., Sullivan, E.J.: Model-based passive ranging. *The Journal of the Acoustical Society of America* **85**(6), 2472–2480 (1989)
- Cébron, D., Vidal, J., Schaeffer, N., Borderies, A., Sauret, A.: Mean zonal flows induced by weak mechanical forcings in rotating spheroids. *Journal of Fluid Mechanics* **916**, 39 (2021)
- Deleplace, B.: Eddy viscosity in rotating fluids: an experimental study - Consequences on the visco-magnetic torque at the Core Mantle Boundary (CMB). Theses, Université Joseph-Fourier - Grenoble I (October 2005). <https://tel.archives-ouvertes.fr/tel-00012097>
- Eckert, S., Gerbeth, G.: Velocity measurements in liquid sodium by means of ultrasound Doppler velocimetry. *Exp. Fluids* **32**, 542–546 (2002) <https://doi.org/10.1007/s00348-001-0380-9>
- Greenspan, H., Howard, L.: On a time-dependent motion of a rotating fluid. *Journal of fluid mechanics* **17**(3), 385–404 (1963)
- Greenspan, H.P.: The Theory of Rotating Fluids. Cambridge Monographs on Mechanics and Applied Mathematics. Cambridge University Press, Cambridge, UK (1968)

- Gough, D., Toomre, J.: Seismic observations of the solar interior. IN: Annual review of astronomy and astrophysics. Vol. 29 (A92-18081 05-90). Palo Alto, CA, Annual Reviews, Inc., 1991, p. 627-685. Research supported by SERC. **29**, 627–685 (1991)
- Hua, Y., Sarkar, T.K.: Matrix pencil method for estimating parameters of exponentially damped/undamped sinusoids in noise. *IEEE Transactions on Acoustics, Speech, and Signal Processing* **38**(5), 814–824 (1990)
- Krasny, L.G., Antonyuk, S.P.: Wave-number estimation in an ocean waveguide. *The Journal of the Acoustical Society of America* **102**(5), 2697–2704 (1997)
- Kay, S.M., Marple, S.L.: Spectrum analysis—a modern perspective. *Proceedings of the IEEE* **69**(11), 1380–1419 (1981)
- Kaplan, E.J., Schaeffer, N., Vidal, J., Cardin, P.: Subcritical thermal convection of liquid metals in a rapidly rotating sphere. *Phys. Rev. Lett.* **119**, 094501 (2017) <https://doi.org/10.1103/PhysRevLett.119.094501>
- Laroche, J.: The use of the matrix pencil method for the spectrum analysis of musical signals. *The Journal of the Acoustical Society of America* **94**(4), 1958–1965 (1993)
- Le Bars, M., Cébron, D., Le Gal, P.: Flows driven by libration, precession, and tides. *Annual Review of Fluid Mechanics* **47**, 163–193 (2015)
- Ledoux, P.: The nonradial oscillations of gaseous stars and the problem of Beta Canis Majoris. *Astrophysical Journal* **114** (1951)
- Mautino, A.R.: Inverse spectral methods in acoustic normal mode velocimetry of high Reynolds number spherical Couette flows. Master’s thesis, University of Maryland (2016)
- Mehl, J.B.: Acoustic eigenvalues of a quasispherical resonator: second order shape perturbation theory for arbitrary modes. *Journal of research of the National Institute of Standards and Technology* **112**(3), 163 (2007)
- Moldover, M.R., Mehl, J.B., Greenspan, M.: Gas-filled spherical resonators: Theory and experiment. *The Journal of the Acoustical Society of America* **79**(2), 253–272 (1986)
- Noir, J., Cébron, D.: Precession-driven flows in non-axisymmetric ellipsoids. *Journal of Fluid Mechanics* **737**, 412–439 (2013)
- Noir, J., Hemmerlin, F., Wicht, J., Baca, S.M., Aurnou, J.M.: An experimental and numerical study of librational flow in planetary cores and subsurface oceans. *Physics of the Earth and Planetary Interiors* **173**(1-2), 141–152 (2009) <https://doi.org/10.1016/j.pepi.2008.11.012>

- Pothérat, A., Horn, S.: Seven decades of exploring planetary interiors with rotating convection experiments. *Comptes Rendus. Physique* (2024) <https://doi.org/10.5802/crphys.233> . Online first
- Philippe, F.D., Roux, P., Cassereau, D.: Iterative high-resolution wavenumber inversion applied to broadband acoustic data. *IEEE transactions on ultrasonics, ferroelectrics, and frequency control* **55**(10), 2306–2311 (2008)
- Pijpers, F., Thompson, M.: Faster formulations of the optimally localized averages method for helioseismic inversions. *Astronomy and Astrophysics* **262**(2), 33–36 (1992)
- Pijpers, F., Thompson, M.: The SOLA method for helioseismic inversion. *Astronomy and Astrophysics* **281**, 231–240 (1994)
- Rajan, S.D., Bhatta, S.D.: Evaluation of high-resolution frequency estimation methods for determining frequencies of eigenmodes in shallow water acoustic field. *The Journal of the Acoustical Society of America* **93**(1), 378–389 (1993)
- Roux, P., Cassereau, D., Roux, A.: A high-resolution algorithm for wave number estimation using holographic array processing. *The Journal of the Acoustical Society of America* **115**(3), 1059–1067 (2004)
- Roy, R., Kailath, T.: ESPRIT-estimation of signal parameters via rotational invariance techniques. *IEEE Transactions on acoustics, speech, and signal processing* **37**(7), 984–995 (1989)
- Roy, R., Paulraj, A., Kailath, T.: ESPRIT—a subspace rotation approach to estimation of parameters of cisoids in noise. *IEEE transactions on acoustics, speech, and signal processing* **34**(5), 1340–1342 (2003)
- Raffel, M., Willert, C.E., Scarano, F., Kähler, C.J., Wereley, S.T., Kompenhaus, J.: *Particle Image Velocimetry - A Practical Guide*. Springer, ??? (2018). <https://doi.org/10.1007/978-3-319-68852-7>
- Schaeffer, N.: Efficient spherical harmonic transforms aimed at pseudospectral numerical simulations. *Geochemistry, Geophysics, Geosystems* **14**(3), 751–758 (2013)
- Su, S., Cébron, D., Nataf, H.-C., Cardin, P., Vidal, J., Solazzo, M., Do, Y.: Acoustic spectra of a gas-filled rotating spheroid. *European Journal of Mechanics-B/Fluids* **84**, 302–310 (2020)
- Scharf, L.L., Demeure, C.: *Statistical Signal Processing: Detection, Estimation, and Time Series Analysis*, (1991)
- Su, S.: *Modal Acoustic Velocimetry in a gas-filled rotating spheroid*. Theses, Université Grenoble Alpes [2020-....] (February 2020). <https://theses.hal.science/tel-02612799>

- Shang, E., Wang, H., Huang, Z.: Waveguide characterization and source localization in shallow water waveguides using the Prony method. *The Journal of the Acoustical Society of America* **83**(1), 103–108 (1988)
- Thompson, M., Brun, A., Culhane, J., Gizon, L., Roth, M., Sekii, T. (eds.): *Helioseismology and Dynamics of the Solar Interior*. Space Sciences Series of ISSI. Springer, ??? (2018)
- Tilgner, A.: Driven inertial oscillations in spherical shells. *Physical Review E* **59**(2), 1789 (1999)
- Trusler, J.P.M.: *Physical Acoustics and Metrology of Fluids*. The Adam Hilger Series on Measurement Science and Technology. IOP Publishing Ltd, ??? (1991)
- Triana, S.A., Zimmerman, D.S., Nataf, H.-C., Thorette, A., Lekic, V., Lathrop, D.P.: Helioseismology in a bottle: Modal Acoustic Velocimetry. *New Journal of Physics* **16**(11), 113005 (2014)
- Vidal, J., Su, S., Cebon, D.: Compressible fluid modes in rigid ellipsoids: towards modal acoustic velocimetry. *Journal of Fluid Mechanics* **885** (2020)
- Zaroli, C.: Seismic tomography using parameter-free Backus–Gilbert inversion. *Geophysical Journal International* **218**(1), 619–630 (2019)

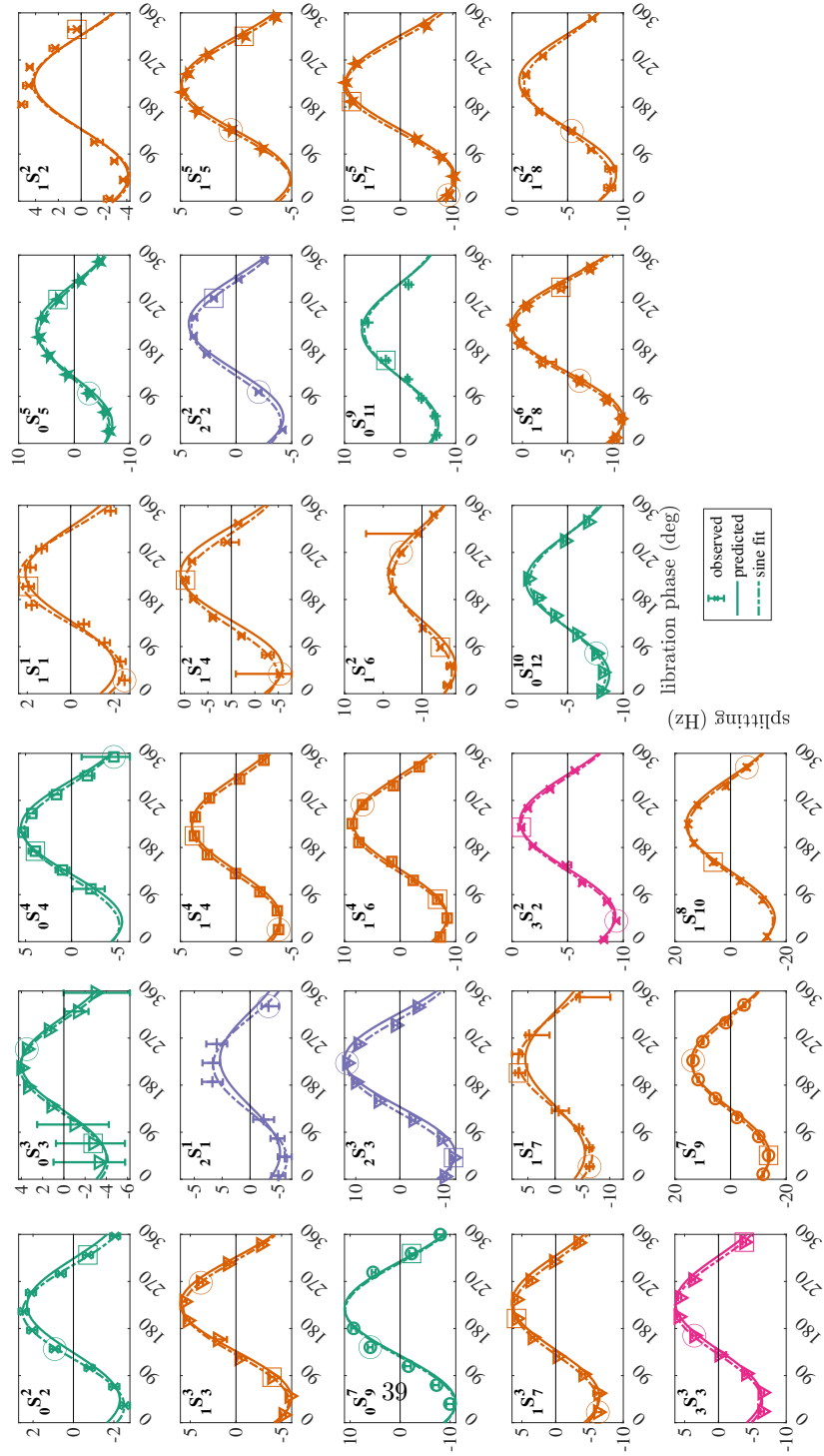


Fig. D4 Frequency splitting (in Hertz) versus libration phase (in degrees) for 27 equatorially symmetric $nS_l^{[m]}$ doublets. Libration parameters: $f_o = 15$ Hz, $f_{lib} = 0.05$ Hz and $\Delta f = 1.5$ Hz. From ten phase-offset 82s-long chirps. Solid line: splitting prediction from Greenspan's theory. Dashed line: least-square sine fit to measured splittings.

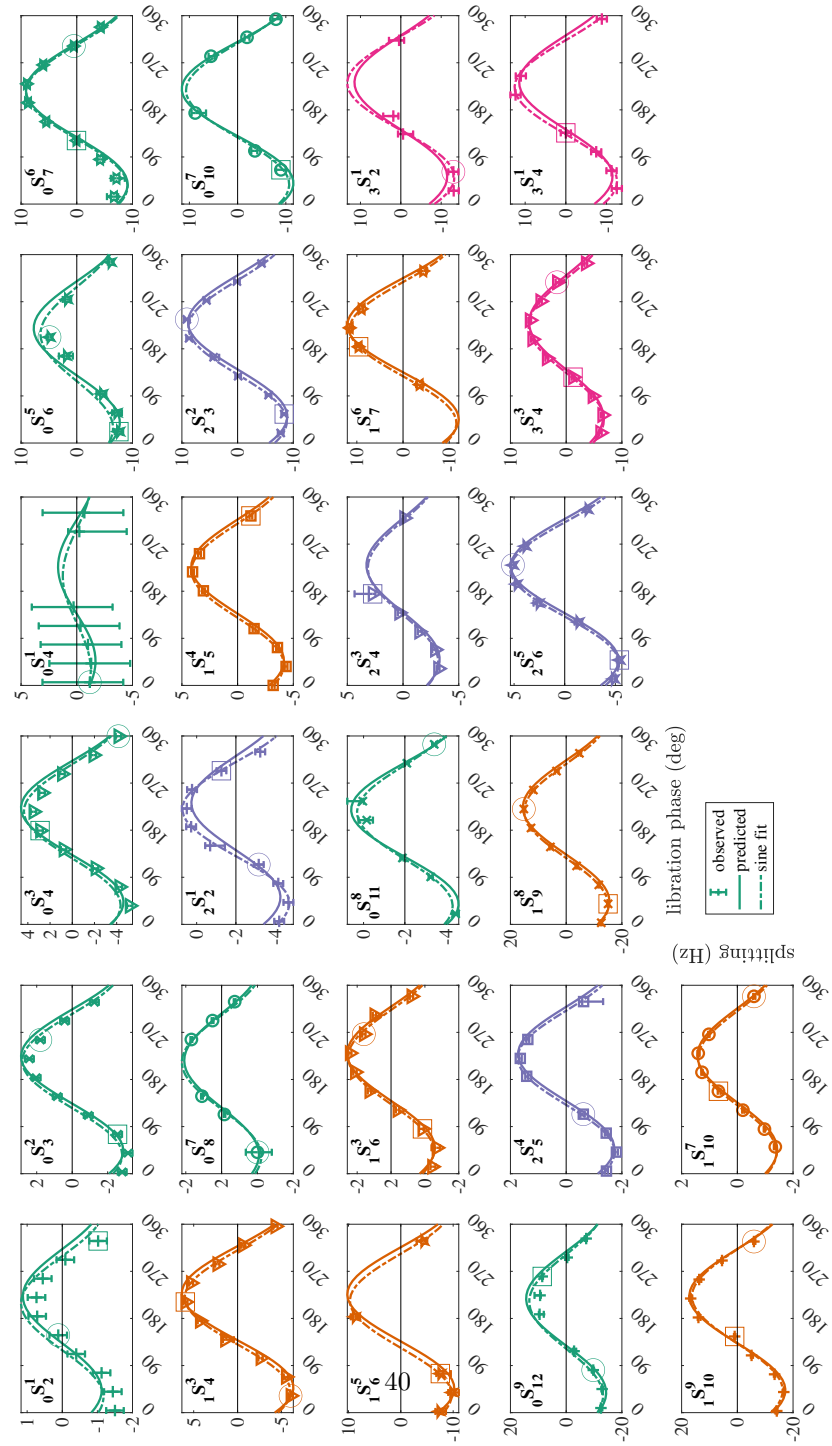


Fig. D5 Same as Fig. D4 for 26 equatorially anti-symmetric $nS_l^{|m|}$ doublets.

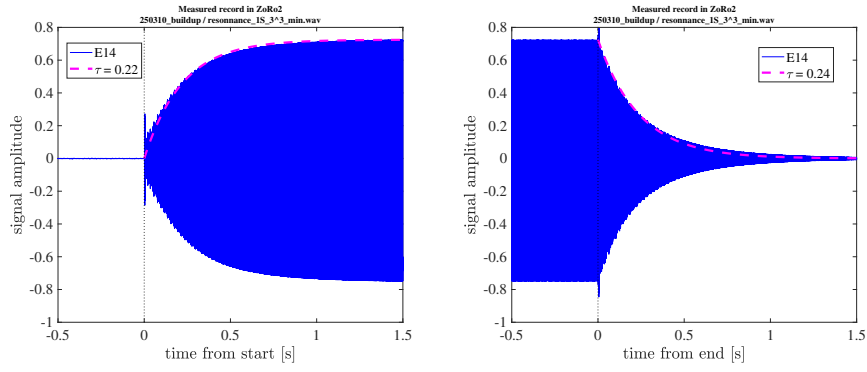


Fig. F6 An example of mode buildup and decay. Doublet $1S_3^3$ was excited, by playing a 10s-long monochromatic sound at its resonance frequency of 2362 Hz. The record at one of the microphones is displayed. (a) Zoom on the growth of the acoustic mode. (b) Zoom on its decay. The envelopes are well fit by $1 - \exp(-t/\tau)$ and $\exp(-t/\tau)$ (magenta dashed lines) with $\tau = 0.22$ s and $\tau = 0.24$ s, respectively.